

Emergence of a Broad-Absorption-Line Outflow in the Narrow-line Seyfert 1 Galaxy WPVS 007¹

Karen M. Leighly¹

*Homer L. Dodge Department of Physics and Astronomy, The University of Oklahoma, 440
W. Brooks St., Norman, OK 73019*

leighly@nhn.ou.edu

Fred Hamann

*Department of Astronomy, University of Florida, 211 Bryant Space Science Center,
Gainesville, FL 32611-2055*

Darrin A. Casebeer

*Homer L. Dodge Department of Physics and Astronomy, The University of Oklahoma, 440
W. Brooks St., Norman, OK 73019*

and

Dirk Grupe

*Department of Astronomy and Astrophysics, Pennsylvania State University, 525 Davey
Lab, University Park, PA 16802*

ABSTRACT

We report results from a 2003 *FUSE* observation, and reanalysis of a 1996 *HST* observation of the unusual X-ray transient Narrow-line Seyfert 1 galaxy WPVS 007. The *HST* FOS spectrum revealed mini-BALs with $V_{max} \sim 900 \text{ km s}^{-1}$ and $FWHM \sim 550 \text{ km s}^{-1}$. The *FUSE* spectrum showed that an additional BAL outflow with $V_{max} \sim 6000 \text{ km s}^{-1}$ and $FWHM \sim 3400 \text{ km s}^{-1}$ had appeared. WPVS 007 is a low-luminosity object in which such a high velocity outflow is not

¹Visiting Professor, Fall 2006 – Spring 2007, The Ohio State University, Department of Astronomy, 4055 McPherson Laboratory, 140 West 18th Avenue, Columbus, OH 43210-1173

expected; therefore, it is an outlier on the M_V/V_{max} relationship. Template spectral fitting yielded apparent ionic columns, and a *Cloudy* analysis showed that the presence of P V requires a high ionization parameter $\log(U) \geq 0$ and high column density $\log(N_H) \geq 23$ assuming solar abundances and a nominal SED for low-luminosity NLS1s with $\alpha_{ox} = -1.28$. A recent long *Swift* observation revealed the first hard X-ray detection and an intrinsic (unabsorbed) $\alpha_{ox} \approx -1.9$. Using this SED in our analysis yielded lower column density constraints ($\log(N_H) \geq 22.2$ for $Z = 1$, or $\log(N_H) \geq 21.6$ if $Z = 5$). The X-ray weak continuum, combined with X-ray absorption consistent with the UV lines, provides the best explanation for the observed *Swift* X-ray spectrum. The large column densities and velocities implied by the UV data in any of these scenarios could be problematic for radiative acceleration. We also point out that since the observed P V absorption can be explained by lower total column densities using an intrinsically X-ray weak spectrum, we might expect to find P V absorption preferentially more often (or stronger) in quasars that are intrinsically X-ray weak.

Subject headings: quasars: absorption lines, quasars: individual ([WPV85] 007)

1. Introduction

Active galaxies, the most luminous persistently-emitting objects in the Universe, are powered by mass accretion onto a supermassive black hole. But gas not only falls into the black hole, it can also be blown out of the central engine in powerful winds, as indicated by the blue-shifted emission and absorption lines observed in the rest-frame UV spectra. Outflows are likely to be an essential part of the AGN phenomenon because they can carry away angular momentum and thus facilitate accretion through the disk. Winds are important probes of the chemical abundances in AGN, which appear to be elevated (Hamann & Ferland 1999). They can distribute chemically-enriched gas through the intergalactic medium (Cavaliere et al. 2002). They may carry kinetic energy to the host galaxy, influencing its evolution, and contributing to the coevolution of black holes and galaxies implied by the observed correlation between the black hole and bulge masses (e.g., Scannapieco & Oh 2004).

¹Based on observations made with the NASA-CNES-CSA Far-Ultraviolet Spectroscopic Explorer. FUSE is operated for NASA by Johns Hopkins University under NASA contract NAS5-32985.

Unfortunately, the nature and origin of AGN outflows remain largely mysterious. Blueshifted absorption lines are the most easily identifiable evidence for outflows. The absorption lines forming in AGN winds are divided into three categories based on line widths: broad absorption lines (BALs; $\text{FWHM} \sim 10,000 \text{ km s}^{-1}$), narrow absorption lines (NALs; $\text{FWHM} \sim < 500 \text{ km s}^{-1}$), and intermediate mini-broad absorption lines (mini-BALs). The relationship between these types of outflows is not well understood, although it appears that BAL outflows are seen only in luminous quasars (e.g., Laor & Brandt 2002), with narrower lines observed in less luminous objects. It is widely believed that the outflows arise from the accretion disk, but the point of origin and acceleration mechanism(s) are not understood (e.g., Proga 2007). In addition, BAL flows are associated with X-ray weakness (e.g., Gallagher et al. 2006), suggesting absorption of the X-ray continuum by very high columns approaching 10^{23} cm^{-2} , that, if also outflowing, strongly constrain acceleration mechanisms.

There is a strong need to measure basic parameters of the flows, but it is difficult. The projected velocity of the BAL is measured directly from the absorption line profile, but the amount of matter and kinetic energy in the outflow is difficult to constrain. Lines are saturated, although not black, implying that the absorbing material only partially covers the source. The geometry and radial extent of the flows are not known. The density is difficult to constrain because most lines arise from permitted transitions and are not very density dependent.

Line variability provides a valuable tool for studying the absorbing gas. For example, variation in absorption-line apparent optical depths can sometimes be attributed to differences in ionization, and the variability time scale can be used to place lower limits on the electron density. This information can then be used to constrain the distance from the nucleus (e.g., Narayanan et al. 2004). In addition, line variability confirms the intrinsic nature of an outflow (Rodríguez Hidalgo et al. 2007). But variations appear to be small in general; mini-BALs become stronger or weaker, and portions of BAL profiles become stronger or weaker. For example, Barlow (1994) found that 15 of 23 BALQSOs spectroscopically monitored showed variations in the BAL ranging from marginal to large, but these variations were all limited to changes in the residual intensity in the trough rather than variations in the velocity structure. Lundgren et al. (2007) studied a sample of 29 BALQSOs that had been observed more than once during the SDSS. They found that 16 were significantly variable, but while they found a few that showed significant variations in velocity structure, there was again a trend for a greater incidence of variability in residual trough intensity. Gibson et al. (2008) report results of a study of variability of 13 BALQSOs observed first in the Large Bright Quasar Survey, and again in the SDSS, yielding a 3–6 year baseline in rest-frame years. All of the quasars vary, but in complex ways, generally appearing as changes in trough depth in discrete regions a few thousand kilometers per second wide. Capellupo et al.

(in prep.) also find relatively modest variability to be common in a sample of 24 BALQSOs observed in multiple epochs. All together, these studies reveal a lack of dramatic variability indicating the flows are generally stable and long term in typical BALQSOs.

WPVS 007 is a low-luminosity Seyfert 1 galaxy ($\alpha_{2000}=00\ 39\ 15.2$; $\delta_{2000} = -51\ 17\ 02$; $z = 0.02882$, $M_V = -18.8$), that is known to exhibit rather peculiar behavior. It was observed 1990 Nov 10–12 during the *ROSAT* All Sky Survey (RASS), where it was found to be a bright X-ray source, although it was observed to have the softest spectrum ever found in an AGN (inferred $\alpha = -7.3$ for $F_E \propto E^\alpha$; Grupe et al. 1995). Subsequent observations (from 1993 Nov 11–13 to the present *Swift* monitoring campaign) have found the object to be consistently X-ray weak (Grupe et al. 1995, 2007, 2008), and the origin of the X-ray weakness is not known. Recently, a *Swift* observation revealed the first detection of this object in hard X-rays (> 2 keV). Although the number of photons observed were small, the data suggest that the source is partially covered by an absorber with $N_H \sim 10^{23}$ cm $^{-2}$ (Grupe et al. 2008).

The UV observations presented in this paper provide a possible explanation of the X-ray transience. We observed dramatic variability in the absorption line properties between an archival *HST* spectrum from an observation in 1996 (discussed in §2) in which the object displays mini-BALs with a maximum velocity of about 900 km s $^{-1}$ and $FWHM \sim 550$ km s $^{-1}$, and a *FUSE* spectrum from an observation in 2003 (§3) in which the object was found to have developed broad absorption lines with $V_{max} \sim 6,000$ km s $^{-1}$ and $FWHM \sim 3400$ km s $^{-1}$ in addition to the mini-BALs. This transformation is the most dramatic ever seen in a active galaxy, and we postulate that the changing absorption observed in the UV is coupled to the transient X-ray behavior. We measure lower limits on the column densities of various ions for both the BAL and the miniBAL (§2 & §3), and use *Cloudy* models to estimate the physical parameters of the absorbing gas. A summary of the paper is given in §5, and appendices describe details of the *FUSE* data analysis. Unless otherwise specified, we assume $H_0 = 73$ km s $^{-1}$ Mpc $^{-1}$, $\Omega_M = 0.27$, and a flat Universe.

2. *HST* Observations

The *HST* observations were conducted 1996 July 30. The *HST* spectra are more than 10 years old, and the data have appeared in the literature several times. Goodrich (2000) shows the spectrum in the region of Ly α and comments on the absorption. Crenshaw et al. (1999) include the data in a study of absorption lines in Seyfert 1 galaxies. They report absorption lines from Ly α , N V, Si IV, and C IV. Constantin & Shields (2003) analyze some of the properties of the UV spectra of NLS1s, and construct a composite NLS1 spectrum of

all publically available *HST* spectra of NLS1s at the time of writing, including WPVS 007. Kuraszekiewicz et al. (2004) analyze all active galaxies observed with the *HST* FOS after the COSTAR correction optics had been put in place. They perform an automated spectral fitting over a broad band pass and present extensive tables of results. However, while this object is included in their paper, their tables do not include information on the high-ionization lines at wavelengths from $\text{Ly}\alpha$ to He II $\lambda 1640$. Dunn et al. (2006) present light curves from *IUE* and *HST* observations of Seyfert galaxies. They find evidence that WPVS 007 varied among four epochs of observation, becoming faintest in the *HST* observation. Finally, Grupe et al. (2007) present *Swift* photometry², showing that WPVS 007 has brightened since the *HST* observation.

Since none of the previously published results present the information we need to do the required analysis of the absorption lines, we extract the spectra from the archive and perform the measurements ourselves.

2.1. Preliminary Analysis

The spectra were extracted from the *HST* Data “Online” website³ for Legacy instruments including the *FOS*. These are final calibration data products, so no recalibration was necessary. The observation log is presented in Table 1.

We first verify the wavelength calibration of the spectra by measuring the wavelengths of Galactic absorption lines. We used Si II $\lambda 1260.3$, C II $\lambda 1334.5$, Al III $\lambda 1670.8$, Fe II lines at 2344.2, 2382.8, 2586.6, and 2600.2Å, and Mg II $\lambda\lambda 2796.4, 2803.5$ (note that vacuum wavelengths are used, as appropriate for the *HST* data). These lines showed that the spectral segments obtained using the G130H, G190H, and G270H gratings were consistent with no anomalous wavelength shifts. There were no convenient Galactic absorption lines available to examine the spectra obtained with the G400H and G570H gratings; since we find no anomalous redshifts or flux offsets (see below) we assume that these spectra are also free of wavelength shifts.

We next merge the spectra starting with the short wavelengths. We examined overlapping regions for flux offsets and found no evidence for any. The final signal-to-noise ratio of the continuum varies from ~ 3.7 at wavelengths shortward of 1600Å (observed frame), to

²The central wavelengths of the *Swift* filters are as follows: *v* 5468 Å; *b* 4392 Å; *u* 3465 Å; *uvw1* 2600Å; *uvm2* 2246 Å; *uvw2* 1928Å (Poole et al. 2008)

³<http://archive.stsci.edu/hstonline/>

22 in near 2700Å, and falling to ~ 9 around 6600Å. We smooth the spectra using a three-point scheme in which the center point is weighted three times the adjacent points. We correct for the Galactic reddening of $E(B - V) = 0.012$ mag (Schegel et al. 1998) using the Cardelli et al. (1989) reddening curve. Finally, we shift the spectrum into the rest frame, adopting the NASA/IPAC Extragalactic Database redshift value of 0.02882.

2.2. Continuum Shape and Reddening

The *HST* spectrum is relatively blue longward of $\sim 2700\text{\AA}$, but becomes significantly redder shortward of that value. We show the spectrum in Fig. 1 overlaid on two comparison spectra. The first comparison spectrum is a mean of *HST* spectra of two NLS1s that were chosen as follows with the intention of finding objects similar to WPVS 007 in properties other than the absorption lines and continuum shape. As discussed in Leighly & Moore (2004), there is significant range of UV emission-line shapes among NLS1s; focusing on C IV, we found that some are rather narrow, strong and symmetric around the rest wavelength, while others are broad, weak and strongly blueshifted. The miniBALs absorb most of the far UV high-ionization emission lines in WPVS 007, but the emission lines profiles outside of the absorption lines appear to be rather symmetric about the rest wavelength. Thus, we sought other NLS1s that had emission lines similar in shape to the portion of the emission lines in WPVS 007 outside of the absorption lines. We found that the WPVS 007 spectrum most closely resembled that of Mrk 493, which had *HST* FOS spectra stretching from $\sim 1160\text{\AA}$ to 6818\AA (observed frame), and Mrk 335, which had *HST* FOS spectra stretching from $\sim 1160\text{\AA}$ to 3300\AA (observed frame) in this far UV region of the spectrum. These two spectra were very similar to one another in slope and emission lines in the overlapping region. These spectra were processed in the same way as discussed above, and then uniformly resampled on a logarithmically-binned wavelength scale that matched the original binning approximately. They were then rescaled to match in flux and averaged over the common-wavelength region. The second comparison spectrum is the FBQS radio-quiet composite spectrum (Brotherton et al. 2001). The composite spectrum has a very similar continuum shape as the Mrk 493–Mrk 335 average, implying that the Mrk 493–Mrk 335 have continua similar to the average quasar. Thus, we make the simplifying assumption that the unreddened intrinsic WPVS 007 spectrum has the same shape as the Mrk 493–Mrk 335 average, and therefore similar to that of the average quasar.

Fig. 1 shows clearly that WPVS 007 is reddened in comparison with the NLS1 mean spectrum and the composite spectrum. The reddening curve appears to be very unusual, however. WPVS 007 and the comparison spectra have essentially the same spectra longward

of $\sim 2700\text{\AA}$, which means that there is either no attenuation in the optical bands, or that there is no wavelength dependence in the attenuation. We develop the reddening curve as follows. We remove Galactic absorption lines and then coarsely rebin the WPVS 007 spectrum and the Mrk 493/Mrk 335 average. We remove regions of prominent emission lines and compute the ratio. The ratio was then fit with a spline model. The ratio appears to be approximately flat shortward of $\sim 1500\text{\AA}$. The ratio appears to have some structure longward of $\sim 3000\text{\AA}$, but it is clear that is caused by higher equivalent-width optical Fe II in WPVS 007, so it was assumed to be 1 longward of $\sim 2700\text{\AA}$. Since the ratio is flat in the optical band, we cannot define a reddening curve in the standard way, relative to $E(B - V)$, as has been done for other AGN by e.g., Crenshaw et al. (2001) and Crenshaw et al. (2002). Instead, we define it relative to 2000\AA , and assume that the optical bands are not attenuated at all. The extinction curve from the spectra, the spline fit and the SMC reddening curve (Prévot et al. 1984) are shown in Fig. 2. The extinction curve in WPVS 007 is unusually steep between 2700\AA and 1700\AA . An attempt was made to reproduce this reddening curve using silicate dust and a distribution of sizes (Weingartner & Draine 2001), but it was unsuccessful (J. Weingartner, P. comm. 2008). While the unusual reddening curve is interesting, we note that it has no effect on the absorption line measurements or analysis.

2.3. Absorption Lines and Profile Analysis

The *HST* spectrum reveals high-ionization absorption lines in N V, C IV, and Ly α . Fig. 3 shows the observed WPVS 007 spectrum (corrected for redshift and Galactic reddening only) between 1185 and 1595\AA in comparison with the average Mrk 335–Mrk 493 spectrum. The presence of these absorption lines was previously noted by Crenshaw et al. (1999). The N V absorption lines are clearly resolved, and we begin our analysis there. Preliminary examination of the lines shows that the absorbing gas must occult both the line-emitting gas and the continuum-emission region since the absorption lines are deeper than the continuum level.

We use a template analysis approach to analyze the absorption lines. Briefly, we create an apparent optical depth template from the N V profiles and then fit that to the C IV and Ly α . The template approach has strengths and weaknesses. A strength is that it is a very straightforward approach. A weakness is that, because of saturation and partial covering, it yields only a lower limit on the column density of the absorbing ions. Nevertheless, the results provide useful constraints on the properties of the absorbing gas.

We develop the apparent optical depth template as follows. The mean Mrk 335–Mrk 493 spectrum was resampled on the wavelength scale of the WPVS 007 spectrum and the ratio

R of the WPVS 007 spectrum and the average spectrum was made. Assuming that the average Mrk 335–Mrk 493 spectrum is a good representation of the unabsorbed WPVS 007 spectrum, R should be 1 outside of the range of the absorption lines, and should be less than one in the region of the absorption lines. The region of the N V absorption lines was isolated, and the apparent optical depths ($\tau = -\ln R$) for the two N V lines were computed. The apparent optical depth profiles for the two lines were essentially indistinguishable implying that absorption is saturated but not black. The shape is commonly understood to be the consequence of a velocity-dependent covering fraction. Since the apparent optical depth profiles were indistinguishable, they could be averaged to produce a mini-BAL template (Fig. 4). The *HST* mini-BAL has an approximate maximum velocity of $V_{max} \sim 900 \text{ km s}^{-1}$ and approximate FWHM of $\sim 550 \text{ km s}^{-1}$.

If the Mrk 335–Mrk 493 mean spectrum is an accurate representation of the unabsorbed WPVS 007 spectrum, we should be able to apply the mini-BAL template to the Mrk 335–Mrk 493 mean spectrum in the region of C IV and Ly α , and reproduce the observed WPVS 007 spectrum in those regions. To investigate this, we fit the spectrum using IRAF `Specfit`. `Specfit` allows a template continuum, and for that we use the mean Mrk 493–Mrk 335 spectrum. For the absorption lines, we use the template developed from the N V line and shown in Fig. 4. We fix the template wavelengths (in `Specfit` treated as a redshift) to the rest wavelengths for each line, and allow the scale factors to be free in the spectra fitting. The best fitting model results are shown in Fig. 5 where we see that the N V template reproduces the C IV and Ly α absorption lines well. The scale factors are given in Table 2, which includes also the *FUSE* spectral fitting results discussed in §3.3. The first column of Table 2 lists the line, the second column gives the vacuum wavelength, the third column is the scale factor of the template including the uncertainty from the spectral fitting, the fourth column is the template used with the exception of the alternative deblending of the *FUSE* spectrum as discussed in §3.3.4, and the fifth column is the estimate of the lower limit of the column density obtained by integrating over the line profile (Eq. 9, Savage & Sembach 1991). The uncertainties in the column densities are proportional to the uncertainties in the scale factors in the fitting, and thus they give only an estimate of the statistical uncertainty. We use the apparent optical depth to estimate the column densities without accounting for saturation and partial covering. Therefore, the column densities are lower limits. Atomic data were taken preferentially from NIST⁴, as well as from The Atomic Line List v2.04⁵ and Morton (1991).

⁴<http://www.physics.nist.gov/PhysRefData/ASD/index.html>

⁵<http://www.pa.uky.edu/peter/atomic>

3. *FUSE* Observation

The observing log for the *FUSE* observation is given in Table 1. The exposure times are split into “day” and “night” exposures. During the day exposures, the satellite is over the portion of the earth in which the earth is lit by the sun. Background from scattered light is somewhat higher during the day exposures, and emission from airglow is stronger. The LIF detectors have larger effective area, and we used both the day and night data from them. The SIC detectors have significantly lower effective area; thus, since WPVS 007 is a somewhat faint AGN, we used only night data from them. Hence, the exposure times reported in Table 1 are shorter for the SIC spectra compared with the LIF spectra.

The *FUSE* data were processed with a modified version of the CalFUSE pipeline version 3.1.8. The modifications involved a reduction of background intensity using a PHA selection. The details are given in Appendix A. The resulting spectra were then merged and smoothed, and the details of that process are given in Appendix B. The resulting spectrum is shown in the top panel of Fig. 6. Identified Galactic absorption lines are labeled below the plot, and the rest wavelengths of common absorption lines are labeled above the plot, regardless of whether they are detected or not. A plausible unabsorbed continuum using the *HST* quasar composite spectrum (Zheng et al. 1997) is included on the graph.

The spectrum clearly shows the presence of broad absorption lines in both high-ionization lines such as O VI $\lambda\lambda$ 1031.9, 1037.6 and low-ionization lines such as C III λ 977. There are a few features that are seen immediately, and they are confirmed by the detailed analysis below. P V $\lambda\lambda$ 1118, 1128 is present. This line from the rather low-abundance element phosphorus has been shown to be characteristic of absorption-line gas with high column density (Hamann 1998). The 1118Å component is clearly deeper than the 1128Å component, suggesting that the lines are perhaps not completely saturated and thus the optical depth is not extremely high, and that partial covering is present. O VI absorption is dominated by a broad and deep trough, but narrow absorption lines similar to the mini-BALs seen in the *HST* spectra are observed in both the O VI doublets and also in Ly β . The mini-BALs are not apparent in the P V troughs.

Before we perform a quantitative analysis of the absorption lines in WPVS 007, we qualitatively compare our spectrum with the *HST* spectrum of a BALQSO LBQS 1212+1445, also shown in the lower panel of Fig. 6. At a redshift of $z = 1.6245$, the *HST* STIS G230L bandpass samples the restframe 600–1200Å band. This comparison is useful because the 10,811-second-exposure *HST* spectrum has considerably better signal-to-noise ratio than our *FUSE* spectrum and thus the lines are easier to identify. In LBQS 1212+1445 we see many of the same lines as in WPVS 007. The P V BALs are clearly present, and the 1118Å component is clearly deeper than the 1128Å suggesting again that the line is not very highly

optically thick and that partial covering is important. The velocity profile has a larger v_{min} but perhaps the same v_{max} for P V. Minibals are present in O VI in both objects, and are also clearly present in C III and N III in LBQS 1212+1445.

3.1. P V Analysis

Analysis of broad absorption lines is very complicated. If the lines are overlapping, the continuum may be difficult to identify, and absorption lines themselves may be blended. The opacity of a line depends on velocity, there may be partial covering that may also depend on velocity, and these cannot be diagnosed directly because of blending. The covering fraction can also differ for different lines and ions. In the case of very high signal-to-noise spectra and unblended lines, these factors may be robustly deconvolved (e.g., Arav et al. 2007), but that is not possible for our relatively blended, low-signal-to-noise spectrum. Therefore, our goal in this section is to use the P V $\lambda\lambda 1117.98, 1128.01$ feature in the *FUSE* spectrum to derive an apparent optical depth profile to be used to fit and deblend the other lines.

As noted in §3.1, P V is clearly seen in the *FUSE* spectrum. Phosphorus has much lower solar abundance than other elements such as carbon, nitrogen and oxygen that commonly produce BALs (e.g., P/C = 0.00093, Grevesse et al. 2007). Therefore, even if those lines are saturated and partial covering is important, it is possible that the P V will not be as optically thick. P V occurs in a region of the spectrum where absorption from other ions is not generally observed, and therefore it may not be subject to severe blending. In fact, the doublet ratio (1118Å component divided by the 1128 Å component) is 2.03, and visual examination of the region suggests that the 1118Å component has a larger apparent optical depth than the 1128Å line. Therefore we first analyze the P V line with the intention of developing a apparent absorption line template from this feature that can be used for the other absorption lines.

Fig. 7 shows an expanded version of the region of the *FUSE* spectrum near P V, after three Galactic absorption lines marked in Fig. 6 had been modeled out. For the continuum, we use a spline fit to the *HST* FOS composite spectrum with an initial factor of 0.7 scaling (the level shown in Fig. 6). We assume that that P V is solely responsible for the absorption between 1095 and 1127Å. Therefore, the termination of the absorption at 1095Å marks the maximum extent of the 1118Å absorption trough, implying a maximum velocity of 6179 km s^{-1} for the broad absorption lines. Using this fact, the region between 1095 and 1127Å can be broken into three parts: one in which the absorption is produced by the 1128Å component only (right on Fig. 7), by the 1118 Å component only (left on Fig. 7), and by a combination of both components (middle on Fig. 7). The extents of the 1128Å

absorption trough and the 1118Å absorption trough are also marked on Fig. 7.

In terms of velocities, we glean the following information from Fig. 7. The velocity profile between zero and -2678 km s^{-1} can be constructed from the 1128Å component (right region in Fig. 7). The velocity profile between 3555 and 6179 km s^{-1} can be constructed from the 1118Å component (left region in Fig. 7). Apparent optical depth profiles from these two regions are easily obtained. But the velocity profile between -2678 and -3555 km s^{-1} must be constructed from the overlap region. The overlap region consists of a superposition of absorption from the -2678 – -3555 km s^{-1} part of the 1128Å trough and the 0 – -854 km s^{-1} part of the 1118Å trough.

Thus our strategy to produce the apparent optical depth profile is as follows. We generate the apparent optical depth by dividing the spectrum by the continuum and taking the logarithm ($\tau_{eff} = -\ln R$). We construct the profile in the 0 – 2678 km s^{-1} band using the 1128Å component, and the profile in the 3555 – 6178 km s^{-1} using the 1118Å component. Then, the two estimates for the 2678 – 3555 km s^{-1} are generated from the overlap regions by subtracting the known component from the apparent optical depth. The overlap region is then the mean of these two estimates. To test the resulting template, we apply it to the continuum to generate the spectrum.

The two uncertainties in this procedure are the ratio of the apparent taus of the two lines and the placement of the continuum. Specifically, we assume that the derived optical depth profile corresponds to the 1128Å component, and the 1118Å component is related by a ratio, to be determined. Initially, we assume that the ratio is the ratio of the gf_{ik} for the two lines, 2.03, appropriate if the absorption lines were optically thin and the covering fraction is unity. The result is shown as the dashed dark grey line in Fig. 7. By definition, the simulated spectrum models the profile well in the low and high velocity regions of the feature that are created by either the 1118 or the 1128Å component each by itself. However, in the overlap region, the synthetic spectrum clearly shows stronger absorption than in the observed spectrum.

There are several possible origins for the discrepancy between the synthetic spectrum and the observed spectrum. First, the continuum level could be lower than assigned. A continuum offset seems unlikely, though, as we set the continuum level at the point where the sharp low-velocity drop on the 1128Å component occurs. More likely, the absorption lines could be saturated ($\tau > 1$) and partial covering could be important so that the ratio between the apparent optical depths of the 1118 component and the 1128 component is less than 2.03 and approaches 1.

Since the ratio of the apparent taus of 2.03 is ruled out, we determine a best fitting ratio

as follows. We define a figure of merit (*fom*), which is the sum of the absolute value of the difference between the simulated spectrum and the observed spectrum in the overlap region. Simulated spectra are generated using a range of apparent tau ratios between 2.03 and 1. The *fom* is a shallow apparently parabolic function of the ratio with a minimum of 1.35. The simulated spectrum using this best fitting apparent tau ratio is shown by the light grey line in Fig. 7. The fit is not perfect, being too shallow for shorter wavelengths and too deep for longer wavelength in the overlap region, but it is clearly better than the fit for a ratio of 2.03. Another possibility is that the apparent tau ratio varies as a function of velocity, with a lower ratio (approaching 1) for low velocities and a higher ratio for high velocities. Since the *fom* has no statistical significance, we estimate the uncertainty on this value by examining at the residuals and determining the point at which the simulated spectrum clearly does not fit the data, yielding a conservative range of 1.15–1.55.

The constraints on reasonable placement of the continuum are fairly tight. The absorption decreases sharply at low velocity, and thus the continuum cannot reasonably be placed very far below the position where this joins the continuum. Likewise, unless we do not see the continuum at all in this object, we cannot place the continuum much higher. We examine the cases in which the continuum was set to be about 4% higher and lower than the original value; this range seemed consistent with the constraints above. The results are very similar. A higher continuum yields a higher maximum velocity and perhaps a slightly better fit for longer wavelengths in the overlap region. A lower continuum yields a lower maximum velocity and a notably worse fit at longer wavelengths in the overlap region. The best *fom* was obtained for the original continuum level, but the differences are not large. Therefore, we use the optical depth profile obtained using the original continuum level, with an inferred ratio of the apparent optical depths of the 1118Å component to the 1128Å component of 1.35. The apparent optical depth profile plot is shown in Fig. 4. The profile has an approximate maximum velocity of $V_{max} \sim 6000 \text{ km s}^{-1}$, and an approximate FWHM of $\sim 3400 \text{ km s}^{-1}$.

As shown in Fig. 6, a set of Fe III transitions occurs near 1126 Å, between the two P V lines. We do not believe that this transition produces significant absorption for several reasons. First, if there were significant absorption from Fe III, the template that we derive would be wrong; yet, as we show below, this template produces an excellent fit for the S IV absorption features at 1063 and 1073 Å. In addition, we noted the similarity to the LBQS 1212+1445 spectrum also shown in Fig. 6. The P V troughs appear narrower and are not blended with one another in that object, and Fe III absorption does not appear to be present. For future use, we measure upper limits on the column density of a multiplet of N II near 1085Å, and one of Fe III near 1126 (Fig. 6) by inserting a *FUSE* BAL template into the model and increasing the normalization until the χ^2 increases by 6.63, corresponding to

99% confidence for one parameter of interest. These upper limits are also listed in Table 2.

3.2. MiniBAL Analysis

The *FUSE* spectrum of WPVS 007 has mini-BALs as well as BALs. These can clearly be seen on O VI and Ly β , and they can also be seen on N III and C III. They are not seen on Si IV or P V. They are distinguished from the BALs by their distinctive shape, most clearly seen on O VI but also because they have a lower-velocity onset than the BALs, as shown in in Fig. 8. In this section we analyze the mini-BALs in the region of Ly β and O VI. We note that although the miniBALs are not blended, we are not able to derive the optical depth and covering fraction as a function of velocity, both because of the poor signal-to-noise ratio and because of a zero-offset problem (described below). Thus, as before, our goal is to produce an apparent tau velocity profile to be used as a template for fitting the other miniBALs.

The mini-BALs are superimposed on the BALs, and thus their profiles are difficult to analyze. To define a pseudocontinuum, we isolate the region of the spectrum between 1020 and 1038Å, and remove the regions of the spectrum containing the mini-BALs from Ly β , and O VI $\lambda\lambda$ 1031.9, 1037.6. We then fit the remainder with a model intended to parameterize the pseudocontinuum. We find that a lorentzian line model plus a constant works well. Next, we need to find the apparent optical depths, generally done by dividing the continuum by the data, and then taking the logarithm. The problem with that procedure for these data is that the spectrum in the region of the mini-BALs dips below zero. This is, of course, not physical, and may be a consequence of residual background subtraction problems, although as shown in figures in Appendix A, the errors are sufficiently large that the data are consistent with zero in the region of the mini-BALs. Therefore, to obtain the template, we add 0.1 to both the continuum model and the spectrum before taking the logarithm. The result is encouraging, as it shows three apparent optical depth profiles that are very similar in shape and depth, although the O VI λ 1032 component has slightly larger apparent optical depth. We resample the Ly β and O VI λ 1038 components to the wavelengths of the O VI λ 1032 component, and compute the mean profile. The result, as a function of velocity, is shown in Fig. 4 in comparison with the mini-BAL template developed from N V in the *HST* spectra, and the *FUSE* BAL profile developed in §3.3. *FUSE* mini-BAL template has approximately the same maximum apparent optical depth as the *HST* mini-BAL; however, this is a lower limit as we had to add a constant to the spectrum in order to compute the apparent optical depth. The *FUSE* mini-BAL seems to perhaps have a sharper onset, a little lower maximum velocity ($\sim 800 \text{ km s}^{-1}$) and a little smaller FWHM ($\sim 470 \text{ km s}^{-1}$), compared with the *HST* mini-BAL, perhaps indicating evolution of this component.

3.3. Modeling the FUSE Spectrum

Now that we have developed apparent optical depth templates for the BAL (discussed in §3.1) and the mini-BAL (discussed in §3.2), we can apply the templates to the remainder of the *FUSE* spectrum. First, though, we emphasize that the template approach has both values and shortcomings. The templates can be used to deblend the complicated absorbed spectrum to identify which lines are present and obtain estimates of the absorption columns of associated ions. But since we have only the apparent optical depth profile, and no information about the covering fraction that may be both velocity and ion dependent, we can only obtain lower limits on the ionic column densities. In addition, we make the assumption that all of the lines have the same apparent optical depth profile, while in reality, the higher ionization lines are sometimes observed to have broader profiles in other objects. We address this final point in §3.3.4.

Our approach is as follows. As for the *HST* spectrum, we fit the spectrum using IRAF *Specfit*. We use the *HST* composite continuum (Zheng et al. 1997) with the normalization fixed at the level shown in Fig. 6 for the continuum. We use the two templates derived in §3.1 and 3.2, fixing the wavelength (treated in *Specfit* as a redshift) to correspond to the rest wavelengths of the absorption lines investigated, allowing only the scale factor (effectively, the apparent optical depth) to be free. To obtain the best fit, we allow the apparent optical depth ratios within multiplets to deviate from the values prescribed by atomic physics. This leads to separate limits on the ionic column densities derived from each line. We discuss three regions of the spectrum separately: the P V/S IV region between 1037.5 and 1135Å, the O VI region between 991 and 1135Å, and the C III/N III/P IV region shortward of 991Å.

3.3.1. P V/S IV Region

We first fit the P V region by itself, between 1090 and 1135Å. The results for the fit of the entire *FUSE* spectra are given in Table 2, where the definitions of the columns were discussed in §2.3. The best fit is shown in Fig. 9. The upper panel shows the final model superimposed upon the spectrum, and the lower panel shows each absorption component.

We next fit the region between 1037.5 and 1135 Å. This region includes a large absorption feature that can plausibly be identified as S IV. This line is composed of three components. The ground state transition has a wavelength of 1062.7Å. The other two transitions from this configuration arise from an excited state with $E_i = 951.43 \text{ cm}^{-1}$, with wavelengths 1072.96 and 1073.51Å. The $g_i f_{ik}$ values for the three transitions are 0.69, 2.09, and 0.23. The latter two lines (the transitions from the excited state) are very close together in wavelength, and

we model them with the $g_i f_{ik}$ -weighted mean wavelength of 1073.07. Absorption from ions in the excited state is clearly present; it can be recognized by the sharp low-velocity onset near 1073Å (Fig. 6). We obtain an excellent fit, as seen in Fig. 6. In particular, the position of the sharp increase in opacity at low velocity matches the spectrum perfectly for both components, verifying that this feature is indeed S IV and that significant absorption from the excited state is present

The undeniable presence of the excited state absorption from S IV is interesting because the energy of the lower level is slightly (0.118 eV) compared with typical values of nebular kT . Population of this level requires $n_e > A_{ki}/q_{ki}$, where $A_{ki} = 7.70 \times 10^{-3}$ is the Einstein A value for the transition from the excited state to the ground state, resulting in the S IV 10.51 μm line, and q_{21} is the collision deexcitation rate, which can be found from the collision strength Υ for this transition. For a nebular temperature of 15,000 K, Saraph & Storey (1999) give $\Upsilon(\text{S IV}) = 8.48$. The resulting critical density is $n_{crit} = 4.7 \times 10^4 \text{ cm}^3$. The fitting reveals that the excited-state line is somewhat stronger than the ground-state line (scale factor 1.54 ± 0.03 vs 1.20 ± 0.05), yielding a ratio of 1.28. At densities above critical, the ratio would approach $g_{ik}(\text{excited})/g_{ik}(\text{ground}) = 2.02$. This suggests that the gas density is near or above the critical density.

3.3.2. The O VI Region

Between 991 and 1037.5Å there is a very broad absorption feature as well as the mini-BALs originating in O VI and Ly β that were discussed in §3.2. O VI is at least partially responsible for the broad feature. However, if the O VI components have the same profile as the P V components, and if O VI were the only contribution to this feature, then the high-velocity decrease in opacity should be observed at approximately 1016Å (the point corresponding to 20% of the maximum opacity of the profile shown in Fig. 6 or 9), rather than stretching to at least 991Å as observed. This may be interpreted as evidence that there are several other ions responsible for absorbing the shorter wavelengths. In this section, we investigate this possibility by including absorption from ions that are conceivably present in the gas. On the other hand, the O VI profile could be alternatively interpreted as being broader than the P V profile; this would not be surprising if true as the profiles of high-ionization lines are frequently found to be broader than those of intermediate ionization lines (Junkkarinen et al. 2001). Therefore, we discuss an alternative deblending in §3.3.4.

In this section, we take the approach that the O VI BAL resembles the P V BAL. It is clear from the discussion above that we will not be able to model the entire feature using the O VI BAL alone, but before adding other lines, we first determine the shortest wavelength

within the feature that we can obtain an adequate fit assuming the presence of only an O VI BAL and miniBAL. We find that we can obtain an adequate fit down to 1018Å, although the fit is not very good between the Ly β and the O VI λ 1032 mini-BAL because the O VI BAL is required to be very deep ($\tau = 4.3$) to model all of the deep absorption present. Decreasing the lower limit of the fitting range further yields larger χ^2 and larger τ for the O VI λ 1032 BAL.

We observe a Ly β mini-BAL, so it is quite possible that a Ly β BAL is also present. We add this component, and find a much improved fit around the mini-BALs. We find that the fit is adequate down to 1012Å; for wavelengths shorter than that, the χ^2 rises precipitously, and the broad Ly β optical depth becomes very large.

S III has resonance and low-lying excited state transitions in this region of the spectrum. The multiplet consists of six components at 1012.50, 1015.50, 1015.57, 1015.78, 1021.11, and 1021.32Å, with corresponding lower level energies of 0, 298.7, 298.7, 833.1, and 883.1 cm⁻¹, and $g_i f_{ik}$ values of 0.042, 0.042, 0.032, 0.053, 0.053, and 0.158, respectively. We model this feature with three BALs centered at 1012.50, 1015.63, and 1021.27Å. We obtain a good fit for wavelengths down to about 1000Å. We note that as we add components to the model, the uncertainties on the optical depths increases; for example, the uncertainty on the S III λ 1015 component is almost as large as the optical depth. When the uncertainty is as large as the measurement, the detection is less than robust. Yet, if we maintain the assumption that the entire broad feature between 991 and 1037.5Å is comprised of features with the same profile as P V, the S III component is necessary.

The S III can account for the deepest part of the trough for wavelengths as short as 1000Å; however, shortward of that wavelength, its opacity drops rapidly. If the broad feature between 991 and 1037.5Å is a blend of lines with the same profile as P V, another ion with resonance wavelength around 1000Å must participate in the absorption. We found a P III resonance triplet that will work. The wavelengths are 998.0, 1001.726, and 1003.6Å, with corresponding gf values of 0.223, 0.668, and 0.473. Including these allows a good fit to the shortest wavelength of this feature at 991Å. The results of this fit are given in Table 2. However, the shortest wavelength component ends up having zero normalization. We obtain an upper limit by increasing the normalization of this component until $\Delta\chi^2 = 6.63$, corresponding to 99% confidence for one parameter of interest. The derived column density upper limit for P III λ 998.0 is comparable to the lower limits for the other two components.

3.3.3. The C III, N III and P IV Region

We finally turn to the region of the spectrum shortward of 991Å that contains C III, N III and P IV. Starting with the region between 955 and 991Å, we see clear evidence for both broad components and mini-BALs for C III and N III, so we begin by adding those lines. The region around N III was fit very well with a BAL and a mini-BAL. In the C III region, the mini-BAL template modeled the region between 972 and 977 angstroms well. However, the feature was too broad to be modeled by the BAL template. Ly γ falls in this region at 972.5Å. We see no evidence for a Ly γ mini-BAL, so we just add a broad component; it turns out that the data cannot constrain a Ly γ BAL and mini-BAL simultaneously, as the signal-to-noise ratio is very low in this region of the spectrum. The Ly γ component allows us to extend the fitting region down to 958Å before experiencing a poor fit. We could not find any other transitions in this region that could significantly add to the opacity. If the entire feature down to 955Å originates in Ly γ or C III alone, and there are no other unidentified transitions, it would imply that the Ly γ or C III absorption profile is broader than the P V profile. This would be surprising if true, given that these lines are from lower-ionization ions than P V. However, we caution that the evidence for this inference is rather weak because the signal-to-noise ratio is very low (the spectrum is almost undetected) and because the region not adequately fit by the C III and Ly γ absorption is rather narrow, only about 4 angstroms wide.

Finally, we seem to see a P IV mini-BAL and BAL near 950Å, so we add a component for each of those, fitting down to 940Å. The mini-BAL is modeled very well with the template set at the P IV wavelength. The rest wavelength of Ly δ is only 0.91Å below P IV, so it is possible that the absorption feature originates in hydrogen instead. Indeed, a comparison of $g_i f_j$ values indicates that the apparent optical depth for Ly δ should be at least 18% that of Ly β . However, substituting Ly δ for the P IV mini-BAL gives a distinguishably poorer fit ($\chi^2 = 789$ for the Ly δ mini-BAL, versus $\chi^2 = 762.5$ for the P IV mini-BAL), and a wavelength offset between the model and the data can be seen. Thus, while the fit is better for the mini-BAL in P IV. This is an odd result, since the miniBAL is clearly not present in P V and S IV, as discussed above. On the other hand, it is worth reflecting that the signal-to-noise ratio in this region of the spectrum is very low (Fig. 17), and therefore any fit results in this region must be taken with a grain of salt.

There are several ions that could contribute to the opacity shortward of 940Å. However, the quasar is essentially undetected in this region, so no meaningful constraints on the column densities can be obtained.

We plot the resulting model and the spectrum in Fig. 9. The results are listed in Table 2. Except for the region between 991 and ~ 1000 Å in the O VI absorption feature, and the

region between 950 and 960Å in the C III/Ly γ absorption feature, the fit is very good. We also plot the individual components of the model in Fig. 9.

3.3.4. *Alternative Deblending*

Fig. 9 shows that we can very nearly successfully fit the whole *FUSE* spectrum using the *FUSE* BAL and mini-BAL templates. But we cannot be confident about our fit in the O VI and C III regions because of the severe blending. We therefore consider an alternative extreme case where all of the absorption between 990 and 1037Å is due to O VI, and all of the absorption between 953 and 978Å is due to C III. The spectra of other BALQSOs often reveal higher velocities in higher ionization lines (e.g., Junkkarinen et al. 2001), so this possibility in the case of O VI is very plausible. Thus, we present an alternative deblending of the blended O VI and C III regions, as follows. We use our successful fits above as a smooth representation of the data and rederive the optical depths and column densities for O VI and C III with this assumption. Note that this procedure underestimates the possible C III optical depth since the model shown in Fig. 9 does not fully account for the absorption between ~ 950 and ~ 960 Å. The net result is a ~ 0.4 dex increase in the column density lower limit in both ions, compared with the values listed in Table 2.

3.3.5. *Column Density Lower Limits*

Using Eq. 9 in Savage & Sembach (1991), we can integrate over the templates to get estimates of the lower limit of the column densities. Those values are given in the fifth column of Table 2. The uncertainties given are proportional to the uncertainties in the scale factors in the fitting, and thus they provide an estimate of only the statistical uncertainty.

4. Discussion

4.1. Cloudy Models

We would like to determine the physical state of the absorbing gas, and investigate other parameters such as the launching radius in order to understand outflows in AGN. While this can be done fairly robustly in some cases where the signal-to-noise ratio is very good and the individual lines in multiplets are resolved (e.g., Arav et al. 2007), it is generally difficult in BALs because the lines are saturated and there is partial covering of the emission source(s).

But the situation is a little better for WPVS 007 because we measure P V in the *FUSE* spectrum, and it does not seem to be completely saturated. We find that we can obtain some interesting and useful limits through analysis of the BALs using the photoionization and spectral synthesis code *Cloudy* (Ferland et al. 1998).

4.1.1. Spectral Energy Distribution

In this section we try to constrain the properties of the absorbers by comparing the results of *Cloudy* models with the column density limits obtained in §3.3.5. *Cloudy* requires as input a spectral energy distribution (SED). As discussed in §2.2, the UV and FUV spectra are clearly reddened, and the X-rays are generally not detected (until recently; see below), so it is not possible to build an SED directly from the WPVS 007 observations. However, as discussed in §2.3, the emission lines of the NLS1s Mrk 493 and Mrk 335 are very similar to those of WPVS 007, and these objects have roughly similar optical luminosity as WPVS 007 ($\log(L_{5500}) = 39.1, 39.4, \text{ and } 40.2$ for WPVS 007, Mrk 493, and Mrk 335, respectively) so as a first approximation, we assume that the intrinsic SEDs are similar. Therefore, we construct a SED for WPVS 007 using data from Mrk 493 and Mrk 335.

Both Mrk 493 and Mrk 335 have been observed by *XMM-Newton* and therefore simultaneous optical/UV and X-ray data are available. Mrk 493 was observed once. During that observation, only the V-band filter was used. The Optical Monitor (OM) image clearly shows the galaxy as well as the bright central AGN, and it is clear that integration of the flux over the nominal *XMM-Newton* extraction aperture of $12''$ will include a significant amount of galaxy light. Yet we need to use this aperture as that is one that is calibrated for conversion to energy fluxes. So we devise an aperture correction using an observation of the bright quasar PKS 0558–504 observed on 2000-05-24. This object is very luminous, and there is no apparent galaxy emission in the V-band image. Using IRAF, we shifted all 10 images using the V-band filter to a common centroid and summed. We determined the FWHM of the PSF from the PKS 0558–504 image to be 3.34 pixels. We then extracted the net flux within one FWHM, considering this to be dominated by the AGN, and within $12''$, using a background annulus between $14''$ and $25''$, and derive an aperture correction of 1.35. We extracted the flux from the Mrk 493 image in a region with a radius of one FWHM and also within $12''$. We then correct for deadtime and coincidence losses using the instructions in the *XMM-Newton* Users Handbook.⁶ Correcting the flux from the small aperture using the correction factor derived from the PKS 0558–504 observation, we find that about 70%

⁶http://heasarc.gsfc.nasa.gov/docs/xmm/uhb/XMM_UHB.html

of the flux within the large aperture originates in the galaxy. We also compare the radial profiles from the Mrk 493 and the PKS 0558–504 images, finding that they agree within the size of the small aperture of 3.34 pixels and verifying extended emission from the galaxy at larger radii. Finally, we extract the flux and correct for the sensitivity degradation using the instructions.⁷ We then scale the *HST* spectrum to match the flux point. The *XMM-Newton* EPIC data from Mrk 493 and Mrk 335 were analyzed in the usual way. Finally each time-averaged spectrum was fitted with a broken power law between 0.3 and 6 keV.

There were two *XMM-Newton* observations of Mrk 335. The first was performed 2000 December 25. During this observation, images were obtained using the V, B, U, and UVM2 filters. The host galaxy spectrum is expected to be red and therefore to not contribute significantly to the flux in the UVM2 filter. Therefore, we use the results of the standard OM analysis, and then scaled the HST spectrum to the UVM2 filter flux. The X-ray data were analyzed in the usual way except that pileup was present in the data from the PN instrument and therefore an annular extraction aperture was used. The spectra were fitted with a broken power law. The second observation was performed 2006 January 3. The OM was operated using the UV grism, and the data were processed in the standard way. The *HST* spectrum was then scaled to the to grism spectrum. The X-ray spectrum was analyzed in the usual way, and fitted to a double broken power law model. Finally, the combined UV and X-ray spectra were sampled in line-free regions to construct SEDs consisting of 10–12 points each.

The three SEDs are very similar. The α_{ox} values for the Mrk 493, and first and second Mrk 335 observations were -1.33 , -1.36 , and -1.32 , respectively. These are very close to the value of -1.22 predicted for WPVS 007 based on the 5500\AA luminosity obtained from the *HST* spectrum and the regression published by Steffen et al. (2006) and their cosmological parameters ($H_0 = 70 \text{ km s}^{-1} \text{ Mpc}^{-1}$, $\Omega_M = 0.3$, $\Omega_\Lambda = 0.7$). Finally, we obtain a merged SED. Since the *HST* spectrum of Mrk 493 extended to the optical band, we started with SED for that object. The Mrk 335 SEDs were rescaled to match the Mrk 493 SED in the near UV. We found that the Mrk 335 points straddled the Mrk 493 points in the X-ray, such that an average would have been very close to the Mrk 493 points. We found that the FUV of the Mrk 335 spectra were very slightly higher than the Mrk 493 points, and appeared to match the optical power law better, so we replaced the three far UV points in the SED with the ones from the scaled Mrk 335 spectrum. We interpolated over the unobservable far UV using a power law between the *HST* and *XMM-Newton* PN spectra. We use the *Cloudy* AGN `kirk`

⁷http://xmm.vilspa.esa.es/sas/7.0.0/watchout/Evergreen_tips_and_tricks/om_time_sensitivity.shtml

spectrum at higher and lower frequencies⁸. The final spectrum has $\alpha_{ox} = -1.28$.

After completing the analysis outlined above, and associated *Cloudy* simulations, Grupe et al. (2008) report the first detection of hard X-rays in WPVS 007. They find evidence for a partially-covered spectrum, and a plausible deconvolution indicates an intrinsic (i.e., unabsorbed) α_{ox} of -1.9 . Therefore we construct an additional continuum spectrum with $\alpha_{ox} = -1.9$ by simply decreasing the flux of the X-ray and higher energy portion of the SED developed above by a factor of 41.3. The two SEDs are shown in Fig. 10.

4.1.2. Simulations and Results for the BALs

Initially we ran *Cloudy* models for the $\alpha_{ox} = -1.28$ continuum for a range of parameters: ionization parameter $-3.5 \leq \log(U) \leq 0.5$, $\Delta \log(U) = 0.25$; density $8.0 \leq \log(n_H) \leq 12.0$, $\Delta \log(n) = 0.5$; column density parameter $\log(N_H^{max})$, defined as $\log(N_H^{max}) = \log(N_H) - \log(U)$, $21.0 \leq \log(N_H^{max}) \leq 24.0$, $\Delta \log(N_H^{max}) = 0.1$ for a total of 4,743 simulations. After determining that the absorption lines are not dependent on the gas density (e.g., see also Hamann 1997), we choose $\log(n) = 10.0$ as the nominal density and extend the simulations to $\log(U) = 1.5$. We also ran the simulations for the $\alpha_{ox} = -1.9$ continuum for that value of the density. We use $\log(N_H^{max})$ rather than just $\log(N_H)$ because a constant value of $\log(N_H^{max})$ probes similar depths in terms of the hydrogen ionization front (e.g., Leighly 2004; Casebeer, Leighly & Baron 2006; Leighly et al. 2007). We used solar metallicity initially.

We followed the approach discussed by Arav et al. (2001) and since used by a number of other investigators. Specifically, we compare our estimates of the column density given in Table 2 with ionic column densities from the *Cloudy* simulations as a function of ionization parameter and column density. We emphasize that since the absorption lines are saturated and partially covered, and since we estimate the column densities from the apparent optical depths, these are the *lower limits* of the column density. Most of the ionic column densities can be extracted from the “column density” output from *Cloudy*. There is one relevant exception: columns from low-lying excited states of metal ions such as S IV. These should be populated at typical BLR temperatures and sufficiently high densities according to their statistical weights $2J + 1$. Thus, the proportion in the ground ($J = 3/2$, the 1062Å component) and fine structure ($J = 5/2$; the 1073Å component) states should be 40% and 60% of the column given by the *Cloudy* output. Interestingly, though, the estimated column densities given in Table 2 show that the proportions of the estimated column density upper

⁸The *Cloudy* AGN kirk spectrum is the *Cloudy* AGN spectrum with the parameters $\log T = 6.00$ $\alpha_{ox} = -1.40$ $\alpha_{UV} = -0.50$ and $\alpha_x = -1$. (Ferland et al. 1998)

limits are 44% and 56%, very close to the expected proportions, and therefore comparing the estimated lower limits with the simulations for both lines would yield indistinguishable results. Thus, for the following analysis, we compare 60% of the *Cloudy* S^{+3} column with the observed column of the 1073Å component.

We first examine the results from the $\alpha_{ox} = -1.28$ simulations. We first consider the BAL deblending that is shown in Fig. 9 using the columns listed in Table 2. As mentioned in §3.1e also measure upper limits on the column density of a multiplet of N II near 1085Å, and one of Fe III near 1126 (Fig. 9) by inserting a *FUSE* BAL template into the model and increasing the normalization until the χ^2 increases by 6.63, corresponding to 99% confidence for one parameter of interest. These upper limits are also listed in Table 2. Fig. 11 shows the ionic column contours from Table 2 on the ionization parameter/ N_H^{max} plane for $\log(n) = 10.0$. Since the column densities we estimate are lower limits, the solutions should lie above and to the right of any curve. Ideally, if the lines were not saturated, the contours would converge in one area of the plot, producing best-fitting values of $\log(U)$ and $\log(N_H) - \log(U)$. The presence of P V implies that lines of similar ions of more abundant species are saturated (Hamann 1998), and therefore we do not expect any region of convergence *a priori*. Interestingly, we do find one in which a majority of the lines converge: for $\log(U) \gtrsim 0.0$, the column densities of a number of the intermediate-ionization ions converge around $\log(N_H) - \log(U) = 23.0$. Notable exceptions are O^{+5} and H^0 , for which simulations show much higher column density than observed at $\log(U) = 0.0$, $\log(N_H) - \log(U) = 23.0$, and S^{+2} and P^{+2} , for which simulations show lower column densities than observed at that point. If the lines are saturated, the observed column densities are lower limits, and therefore the O^{+5} and H^0 columns may be consistent with the other lines at $\log(U) = 0.0$, $\log(N_H) - \log(U) = 23.0$, but the P^{+2} , and S^{+2} would not be, because the lower limit exceeds the simulated column densities at that point.

We note that as expected, there is little dependence on the density for values in the range $9.5 \leq \log(n) \leq 11$. The column densities of P^{+2} are lower at very low densities and increase as the density is increased, but only for the highest values of $\log(N_H^{max})$. At the highest densities, lower-ionization columns increase, primarily at the highest values of $\log(N_H^{max})$. In all cases, the differences are small, and we cannot obtain a markedly better agreement with the observations by assuming very high or very low densities.

As discussed in §3.3, while the deblending in terms of the *FUSE* BAL template presented in Fig. 9 matches the spectrum well, it is possible that the higher-ionization lines have a broader profile, and O VI dominates the region between 990Å and 1037Å, and therefore we presented the alternative deblending in §3.3.4. The alternative deblending does not attribute any measurable opacity to hydrogen, P^{+2} , or S^{+2} (since the onset of absorption for these

lines cannot be clearly seen in the spectrum), but instead attributes the absorption to O^{+5} between 990\AA and 1037\AA , and to C^{+2} between 953 and 978\AA . Using these alternative fitting results, we generate the contour plot as before (Fig. 11, right side). Now we see that all measured ions and upper limits are consistent near $\log(N_H) - \log(U) = 23.0$ and $\log(U) \geq 0$, except for O^{+5} which is clearly saturated.

We perform the same procedure as above for the simulations using the $\alpha_{ox} = -1.9$ continuum (Fig. 10 middle panel). The results are rather similar in that there is again a region of convergence for the intermediate-ionization ions, and in this region, the columns O^{+5} and H^0 are much larger than our inferred lower limits, while the columns of P^{+2} and S^{+2} are much lower than our inferred lower limits. The principal difference is that the location of the convergence of many ionic columns occurs at a lower value of N_H^{max} . Our nominal best solution for this continuum is $\log(U) = 0.0$ and $\log(N_H) - \log(U) = 22.0$. This result can be understood by considering that intermediate-ionization ions are created at a smaller column density in gas illuminated by an X-ray weak continuum than in gas illuminated by an X-ray normal continuum because the X-ray weak continuum is unable to produce the usual higher-ionization ions (e.g., Leighly et al. 2007). Most of the observed absorption lines (except O VI) are from intermediate-ionization ions.

Quasars are often inferred to have enhanced metallicities (e.g., Hamann et al. 2002). The hydrogen column densities derived above are large, and as will be shown in §4.2, challenge outflow models. Inferred hydrogen column densities should be lower if the metallicity is enhanced. We therefore try a $\alpha_{ox} = -1.9$ model with $Z = 5$ (that includes helium enhanced by a factor 1.29 and nitrogen enhanced by a factor of 25; Hamann et al. 2002). The results are shown in the lower panel of Fig. 11. Here, the intermediate-ionization ions converge for $\log(U) = 0$ at $\log(N_H) - \log(U) = 21.6$.

Since we expect that partial covering is strongly influencing our analysis, the fact that the data and models converge for many of the ions at particular points in these graphs seems somewhat surprising. This convergence could be coincidental; alternatively, it could really be the case that only O VI and H I are very saturated and the intermediate-ionization ions seen in the *FUSE* spectrum are not very saturated. This idea is supported by the fact that the upper limits for the undetected absorption lines Fe III and N II are seen in Fig. 11 to lie either in the region of convergence, or not very far above it. Therefore, we use the column densities of convergence at $\log(U) = 0$ (specifically, $\log(N_H) = 23.0$, 22.2 , and 21.6 for the $\alpha_{ox} = -1.28$ set of simulations, the $\alpha_{ox} = -1.9$ simulations, and the $\alpha_{ox} = -1.9$ and $Z = 5$ simulations) for discussion in the rest of the paper, emphasizing that these columns are lower limits. The transmitted continua for these cases are shown in Fig. 10.

Further analysis reveals some interesting facts about these solutions. First, the choice

of ionization parameter is driven by P^{+4} ; specifically, the ionization parameter must be sufficiently high to produce a sufficient column of P^{+4} to match the data. This means that the ions seen in the UV spectra are the tip of the ion iceberg, since these ions dominate gas with much lower ionization parameters than $\log(U) = 0$. That is, for most elements, most of the atoms are in higher ionization states, including C^{+3} and N^{+4} , but also much higher ionization states, indicating that most of the opacity is in the extreme UV and soft X-ray band. That this is true can be seen in the absorbed spectra shown in Fig. 10; much of the continuum in the extreme UV and soft X-ray is absorbed by gas with this ionization parameter and column density.

In summary, we find that we can explain the *FUSE* spectrum, in particular, the presence of absorption from the low-abundance element phosphorus, with a highly ionized ($\log(U) \geq 0.0$), high column density absorber. We need to make the assumption, though, that the high-ionization lines such as O VI are much broader than the intermediate-ionization line P V. Strongly enhanced abundance of phosphorus is not needed because some lines are saturated, although they are not black because partial covering is important. This is essentially the same result found by Hamann (1998) for the quasar PG 1254+047 (see also Hamann et al. 2001). A subtlety explored here is the dependence of the result on the spectral energy distribution. The primary distinction for the X-ray weak $\alpha_{ox} = -1.9$ simulations is that the simulated column densities of the intermediate-ionization ions including P^{+4} are large enough to match the observed column lower limit at significantly lower values of N_H . As noted above, this occurs because the X-ray-weak continuum is not able to create high-ionization ions, and therefore the gas cools via transitions of intermediate-ionization ions even in front of the helium ionization front (the hydrogen ionization front for the $\alpha_{ox} = -1.9$ continuum is located beyond $\log(N_H) - \log(U) = 24$). Thus, while partial covering implies that the column densities are probably larger than inferred from the apparent line optical depths, and the outflows are still massive enough to challenge radiative-line driving as the acceleration mechanism (e.g., Hamann et al. 2001, see also §4.2), the situation is not as extreme if the continuum is X-ray weak, because sufficient P V can be produced at significantly smaller (factor of 6 for solar abundances, factor of 25 for enhanced abundances) column densities.

4.1.3. Implications for the X-ray Spectra

As discussed in §1, WPVS 007 has peculiar X-ray properties. Its flux during the *ROSAT* All Sky Survey was typical for an AGN of its luminosity. Then, many subsequent observations found it to have nearly disappeared from the X-ray sky. Could the variable UV absorber be responsible for the X-ray behavior?

As discussed in Grupe et al. (2008), WPVS 007 has been detected recently twice in X-rays: first, by *Chandra*, which observed 10 soft photons from the object (also, Vaughan et al. 2004), and more recently by *Swift*, which observed a total of $35.7_{-6.7}^{+6.4}$ photons, including the first hard (> 2 keV) X-rays. Moreover, the *Swift* spectrum suggests partial-covering; that is, the spectrum appears to have a soft component, and a separate absorbed hard component (Grupe et al. 2008). As discussed in §4.1.2, the column densities and ionization parameters required to attain sufficient P^{+4} indicate considerable opacity in the extreme UV and soft X-rays, as shown in Fig. 10. We can use those absorbed continua to predict the X-ray count rates, as follows. We first normalize the continua to the blue optical part of the 1995 *HST* spectrum, noting that the normalization is somewhat uncertain since the UV emission has been observed to change by a factor of 1.5 over the last several years (Grupe et al. 2007, 2008). We convolve the X-ray portion of the continuum with the Galactic column density ($N_H(\text{Gal}) = 2.84 \times 10^{20} \text{ cm}^{-2}$) where the opacity is given analytically by Morrison & McCammon (1983). We fold the results with the ancillary response files (essentially the effective area or quantum efficiency curve) generated for the *Chandra* and *Swift* observations. Integrating over the X-ray band pass (taken to be 0.3–10 keV) yields count rates. Finally, multiplying by the effective exposure time (9300 seconds for the *Chandra* observation, and 85,508 seconds for the *Swift* observation) yields the number of photons predicted to have been detected. The results are given in Table 3.

These simulations show that, as expected from Fig. 10, the predicted absorbed X-ray flux is much lower than the direct flux. The largest decrease (factors of 31 and 39 for the *Chandra* and *Swift* observations) is found for the $\alpha_{ox} = -1.28$ continuum, because the *Cloudy* simulations discussed in §4.1.2 require the largest N_H to attain the ion column densities required to produce the absorption lines. However, the resulting count rates are much larger than observed: for example, only 10 photons were observed in the *Chandra* observation, and these absorbed continua predict 454 photons for the absorbed X-ray spectrum. Moreover, as seen in Fig. 10, these would have been hard X-ray photons ($E > \sim 2$ keV), while the observed *Chandra* photons were all soft ($E < \sim 2$ keV). The same is true for the *Swift* observation: the predicted number of photons is 325, while only 35.7 source photons were observed.

The correspondence is much better for the $\alpha_{ox} = -1.9$ models. Again, the predicted absorbed flux is much lower than the direct flux, but by only by factors of 5–8 for the solar metallicity model, and 7–11 for the $Z = 5$ model. This difference is due to the reduction in the lower limit of the column density required to produce the FUV line opacity, as discussed in §4.1.2. Interestingly, the $Z = 5$ metallicity model requires a smaller column density, yet predicts a lower X-ray flux. This is due to the increased opacity in the soft X-rays from the additional metals. The count rates are still somewhat too high; for example, the predicted *Swift* spectrum has 70 counts for the $Z = 5$ model, and only 35.7 were observed.

But considering the uncertainty on the absolute normalization and the fact that the derived columns are upper limits, the agreement within a factor of two is remarkably good.

Finally, it should be noted that the predicted X-ray spectra shown in the lower two panels of Fig. 10 are hard, absorbed spectra but with a recovery toward soft X-rays that would be able to be fitted by partial covering models. Thus, these models would correspond well to the *Swift* spectrum (Grupe et al. 2008) but would not explain the *Chandra* spectrum in which no hard X-rays were observed.

These estimates show that if the intrinsic α_{ox} is -1.28 , the gas responsible for the UV absorption lines would have been insufficient to explain the X-ray weakness by absorption in the same gas. However, if the intrinsic α_{ox} is -1.9 , as indicated by the *Swift* spectrum, the same gas could have been responsible for the UV absorption lines, the absorbed component of the X-ray spectrum, and also potentially the X-ray soft excess. There are many caveats, however. The primary one is that the *FUSE* and *Swift* observations were separated by four years, and since this is clearly an evolving system, there is no guarantee that the X-ray and far UV spectra were the same as observed. In addition, the P V absorption profile shows signs of saturation plus partial covering, implying that the real column densities are larger than the lower limits discussed here. Furthermore, while the idea that the UV and X-ray absorption occur in the same gas is simple and attractive, there is no physical requirement that that be the case, since the X-ray and UV emission may not be produced in the same region of the central engine (e.g., Gallagher & Everett 2007).

4.1.4. Simulations and Results for the MiniBALs

We next consider the mini-BALs. We combine the results for the *HST* and *FUSE* observations, noting that these were not simultaneous and it is possible that the apparent optical depths changed between the two observations. Following the same procedure as above, we produce the contour plot shown in Fig. 12, showing again the results for three cases: $\alpha_{ox} = -1.28$, $\alpha_{ox} = -1.9$, and $\alpha_{ox} = -1.9$ with $Z = 5$. An important constraint on the mini-BALs is that we do not detect the mini-BALs in either P⁺⁴ or S⁺³ (Fig. 8). We obtain upper limits on the mini-BAL columns of these ions by including the mini-BAL template in the spectral-fitting model, and increasing its opacity until the χ^2 increases by 6.63, corresponding to 99% confidence for one parameter of interest. Those values are listed in Table 2.

Considering first the $\alpha_{ox} = -1.28$ continuum, we find that we obtain a reasonable solution for $\log(U) \geq \approx -0.3$ and a $\log(N_H) - \log(U)$ lower limit of 22.8, corresponding to

a $\log(N_H)$ lower limit of 22.5. This solution is consistent with the upper limit on mini-BAL column densities of both P^{+4} and S^{+3} . This solution indicates that the Ly α , C IV and N V absorption lines are strongly saturated.

We next present the results for $\alpha_{ox} = -1.9$ (middle panel of Fig. 12). We find a rough correspondence for $\log(U) \geq 0.5$ and $\log(N_H) - \log(U)$ lower limit of 22.2 corresponding to a $\log(N_H)$ lower limit of 22.8. Again, Ly α , C IV and N V absorption lines are strongly saturated, consistent with the observed absorption line intensity ratios (§2.3). However, this solution is not consistent with the upper limit on mini-BAL column densities of both P^{+4} and S^{+3} .

Finally, for $\alpha_{ox} = -1.9$ and $Z = 5$, we find a rough correspondence for $\log(U) \geq 0.5$ and $\log(N_H) - \log(U)$ lower limit of 21.5 corresponding to a $\log(N_H)$ lower limit of 22.0. In this solution, however, the column densities of P^{+4} and S^{+3} would exceed the upper limits. Thus, it does not appear to be possible to produce the miniBALs and upper limits with either of the two continua we are considering.

It may be possible to reconcile the column density constraints from the detections and the upper limits if the upper limits on the unobserved lines are too low. As discussed in Hamann et al. (2001), this could be true if the covering factor is higher for strong/detected lines than for weak lines. In a patchy absorber with a range of optical depths (see, e.g., Fig. 6 in Hamann et al. 2001), strong lines could have large optical depth over a larger area, while weak ones could still have $\tau > 1$ but over a smaller area, leading to a lower observed equivalent width. Our assumption of complete coverage for all lines would then lead to a too-low upper limit on the undetected weak lines.

4.2. Luminosity Dependence and Launch Radius

As discussed in §1, outflows are common in AGN, but their nature differs between high and low luminosity objects. High velocity outflows are generally limited to high luminosity objects, while lower luminosity objects have typical outflow velocities of only $< 10^3 \text{ km s}^{-1}$. The dependence of absorption on other AGN parameters has been systematically investigated using a sample of low-redshift ($z < 0.5$) quasars with M_V between ~ -21 and ~ -27 by Brandt et al. (2000) and Laor & Brandt (2002). A primary result of Brandt et al. (2000) is that there exists a significant correlation between α_{ox} and C IV absorption-line equivalent width, suggesting that the primary cause of X-ray weakness is absorption, with a continuum of absorption columns connecting unabsorbed objects to BALQSOs. In Laor & Brandt (2002) ideas associated with that continuum of absorption columns were further developed;

in particular, the question of what makes a soft X-ray weak quasar a BALQSO was addressed. WPVS 007 is soft X-ray weak, both as a consequence of absorption, and it is apparently also intrinsically soft X-ray weak (Grupe et al. 2008). As shown in this paper, it had broad absorption lines during the *FUSE* observation in 2003. In this section, we compare some of our results with those of Brandt et al. (2000) and Laor & Brandt (2002).

One of the principal results of Laor & Brandt (2002) is that there is a strong dependence of outflow properties on luminosity. Specifically, there are strong positive correlations between the C IV equivalent width and V_{max} , the outflow maximum velocity, with the optical luminosity M_V for soft X-ray weak quasars, and at any luminosity, soft X-ray weak quasars had the largest equivalent widths and maximum velocities. As discussed by Laor & Brandt (2002), this behavior is consistent with outflow scenarios for outflows driven by either dust or line opacity.

We compare WPVS 007 with the quasar sample from Laor & Brandt (2002) in Fig. 13. The M_V value of -19.8 was derived from the dereddened, restframe *HST* spectrum using $H_0 = 50 \text{ km s}^{-1} \text{ Mpc}^{-1}$ and $q_0 = 0.1$ so as to be consistent with the other data. The straight line in that graph shows the best fit to the soft X-ray quiet quasars given by Laor & Brandt (2002); they note that it suggests an upper envelope as would be expected from radiation-driven winds. The filled star labeled WPVS 007 BAL is taken from the *FUSE* BAL template derived in §3.3. The $V_{max} = 6179 \text{ km s}^{-1}$ for that absorption line is seen to be a factor of 13 in excess of the value expected if the regression holds for low luminosity objects. We note that most of the data shown in Fig. 13 were derived from C IV absorption lines, and it is not clear that the P V absorption line should have the same profile. However, as shown by Junkkarinen et al. (2001), P V absorption is typically better fit by templates derived from Si IV, and templates from Si IV tend to be narrower than templates from C IV. This evidence, plus the fact that we infer that the O VI absorption profile in WPVS 007 is most likely significantly broader than the P V profile (§3.3.2 & 4.1.2), indicates that the point shown in Fig. 13 for the BAL may be a lower limit, and the discrepancy between that point and the Laor & Brandt (2002) regression may be even larger. We also plot the V_{max} for the mini-BALs, where we show the mean of the values for the *HST* mini-BAL (§2.3) and the *FUSE* mini-BAL (§3.2). That V_{max} is very near the Laor & Brandt (2002) regression, indicating the outflow maximum velocity that might be expected for this relatively low-luminosity object.

Such a large maximum velocity in a low-luminosity object such as WPVS 007 may cause problems for acceleration models. In a radiative-line-driving scenario, fundamental limits can be placed by simply considering $F = ma$ where the force of the radiative line driving, essentially turning continuum luminosity into wind momentum, is opposed by the

force of gravity due to the black hole. The $F = ma$ equation, with the acceleration $a = v(dv/dr)$ integrated to get the terminal velocity, and converted to parameters suitable for this situation, is presented as Equation 3 in Hamann (1998) (also, Hamann et al. 2001):

$$V_\infty \approx 9300 R_{0.1}^{-1/2} \left(\frac{f_{0.1} L_{46}}{N_{22}} - 0.1 M_8 \right)^{1/2}$$

where $R_{0.1}$ is the launch radius in units of 0.1 pc, $f_{0.1}$ is the fraction of the total flux incident on the flow that is absorbed or scattered by the wind, relative to 10%, L_{46} is the luminosity in terms of $10^{46} \text{ erg s}^{-1}$, N_{22} is the column density relative to 10^{22} cm^{-2} , and M_8 is the black hole mass in terms of $10^8 M_\odot$.

To use the Hamann (1998) equation, we need an estimate of the black hole mass. We estimate the black hole mass using standard methods using the *HST* spectrum. We model the region including $\text{H}\beta$ with a linear continuum, an Fe II template, a Lorentzian profile for broad $\text{H}\beta$, and two Gaussians for O III constrained to have flux ratios of three to one, equal width, and fixed separation. We also use a Gaussian for the NLR component of $\text{H}\beta$, fixing the flux to be one tenth that of [O III] $\lambda 5007$ (Cohen 1983; Leighly 1999). The [O III] lines are slightly blueshifted with respect to the peak of $\text{H}\beta$, as is sometimes found in Narrow-line Seyfert 1 galaxies (e.g., Aoki et al. 2005; Bian et al. 2005), and relative to lower-ionization narrow-line region lines, and therefore we fix wavelength of the narrow component of $\text{H}\beta$ to match that of broad $\text{H}\beta$. The resulting fit is very good; e.g., substituting a Gaussian for the Lorentzian to model broad $\text{H}\beta$ yields a much worse fit. The width of $\text{H}\beta$ is measured to be 1190 km s^{-1} . We obtain the rest frame flux at 5100\AA from the *HST* spectrum ($1.1 \times 10^{-14} \text{ erg s}^{-1} \text{ cm}^{-2} \text{ \AA}^{-1}$). We compute the broad-line region radius using the regressions found by Bentz et al. (2006) using the flux and a luminosity distance of 126.2 Mpc using their (inferred) cosmological parameters of $H_0 = 70 \text{ km s}^{-1} \text{ Mpc}^{-1}$, $\Omega_M = 0.27$, and $\Omega_\Lambda = 0.73$. That is found to be $\log(R_{BLR}) = 1.062$ in units of light-days. Finally, we compute the dispersion of the $\text{H}\beta$ line profile obtained after subtracting the other fitted components, and referring to Collin et al. (2006), we use a scale factor of 1.2 to yield a black hole mass of $4.1 \times 10^6 M_\odot$.

We estimate the bolometric luminosity by integrating over the *Cloudy* continuum spectra discussed in §4.1.1 after they had been normalized to match the rest-frame optical spectrum (recall, as discussed in §2.2, the UV continuum is heavily reddened). These are given in Table 4. We obtain a rough estimate of the fraction of the continuum absorbed in the wind by integrating over the absorbed continuum and comparing with the unabsorbed value. This includes only thermal velocity for the lines, so it provides a lower limit on the fraction of the continuum able to accelerate the wind. These estimates vary from $f_{0.1} = 4.1$ for the

$\alpha_{ox} = -1.28$ continuum, from which we infer the highest column density, to $f_{0.1} = 0.67$ for the $\alpha_{ox} = -1.9$, $Z = 1$ case and $f_{0.1} = 0.44$ for the $\alpha_{ox} = -1.9$, $Z = 5$ case, from which we require lower column densities, as discussed in §4.1.2. We emphasize again, though, that only lower limits on the column densities were obtained. Finally, using the opacity profile in Fig. 4, we conservatively estimate a terminal velocity of about $4,000 \text{ km s}^{-1}$; that is, we observe measurable opacity to about $6,000 \text{ km s}^{-1}$, but the opacity has decreased significantly from the maximum by $4,000 \text{ km s}^{-1}$. It should be noted, however, that as discussed in previously in this section, and in §3.3.4, the O VI absorption line may have a much higher terminal velocity, up to $12,000 \text{ km s}^{-1}$.

The estimate of the launch radii for the $\alpha_{ox} = -1.28$ model, the $\alpha_{ox} = -1.9$ model, and the $Z = 5$ $\alpha_{ox} = -1.9$ model are given in Table 4. For the $\alpha_{ox} = -1.9$, $Z = 1$ model, we obtain a negative radius, which means that the momentum of the absorbed continuum is not sufficient to counteract gravity, and an outflow would not be predicted. The largest outflow radius is found for the $\alpha_{ox} = -1.9$, $Z = 5$ model, of $R_{0.1} = 0.0070$, or $7 \times 10^{-4} \text{ pc}$, or $2.16 \times 10^{15} \text{ cm}$. A $4.1 \times 10^6 M_{\odot}$ black hole has a Schwarzschild radius of $R_S = 1.2 \times 10^{12}$, implying that the launch radius is on the order of $1780R_S$.

The radius of the broad line region was estimated above to be $\log(R_{BLR}) = 1.062$, corresponding to $3 \times 10^{16} \text{ cm}$, about 14 times the inferred launch radius. This could be a problem for the radiative-line-driving model, since the broad absorption-line region is thought to lie at a larger radius than the broad emission-line region. This may imply that a magnetic component of acceleration is necessary (e.g., Bottorff et al. 1997; Everett 2005). On the other hand, the radius of the observed BAL gas may be much larger than the launch radius, and the BAL simply does not intercept the line of sight until it reaches the BLR or beyond.

4.3. Absorption Variability in WPVS 007

Variability in broad absorption lines in quasars is common. Usually, changes in apparent optical depth, coupling real changes in opacity and covering fraction, rather than changes in velocity profile are observed. Recently, more dramatic changes have been reported (e.g., Lundgren et al. 2007; Gibson et al. 2008, and references therein), although it is important to note that these variability studies were limited to known BALs. The BAL in WPVS 007 is distinct in several ways. First, it is one of the very few known cases in which a BAL flow appeared; other possibly similar examples have been found in the quasars TEX 1726+344 (Ma 2002) and J105400.40+034801.2 (Hamann et al. 2008). Second, as shown in Fig. 13, it has quite a low luminosity for the maximum velocity of the outflow.

The development of the BAL in WPVS 007 may be associated with its low luminosity. WPVS 007 has a small black hole mass and correspondingly small central engine, emission- and absorption-line regions. For example, LBQS 1212+1445, the comparison object shown in Fig. 6, has an outflow with similar maximum velocity, but with $M_V = -27.6$, it is 100 times more luminous, and therefore the emission regions are expected to be 10 times larger.

Currently, we have only two epochs of UV observations of WPVS 007: one with only mini-BALs (the 1996 *HST* observation), and one with both mini-BALs and BALs (the 2003 *FUSE* observation). Thus, we can only speculate about the origin of the variability. In other variable objects, a favored explanation is generally a change in covering fraction. Thus, perhaps WPVS 007 always had a BAL outflow, but rotation of the accretion disk (assuming the BAL arises from a disk wind) may have simply rotated it into the field of view. This argument is used to explain variability in quasar-luminosity BALQSOs in Gibson et al. (2008) over 3–6 years, and thus it would certainly be a viable explanation for change in WPVS 007 with its lower luminosity, thus, smaller size- and time-scales, and longer interval between observations.

Another, perhaps more exciting possibility is that the BAL outflow developed over the time scale of seven years. The observations were separated by 2.22×10^8 s in the rest frame. If the velocity of the bulk of the outflow was $4,000 \text{ km s}^{-1}$, then it could have covered a distance of 8.9×10^{16} cm in the interval between the observations. As discussed by Hamann et al. (2008) and references therein, the high-ionization absorption plausibly occurs just outside the corresponding broad emission line radius. We estimate the size of the BLR in WPVS 007 to be 3×10^{16} cm, and thus there would have been just sufficient time for the absorbing flow to cover the BLR. In an object 100 times more luminous, such as LBQS 1212+1445, and similar outflow velocity, it would have taken ten times longer, or about 70 years. So WPVS 007 may be unique in that we observed the development of a BAL. Since we can observe such extreme evolution on human time scales, WPVS 007 is an important object for understanding BAL winds physical conditions and driving mechanisms.

This argument is compelling, but cannot simply explain both the X-ray and UV variability. WPVS 007 was already X-ray weak by the time of the *HST* observation in which only the miniBAL was observed. So the emergence of the UV BAL into the line of sight by the *FUSE* observation could not have been directly associated with the X-ray absorption. Rather, it is possible that the X-ray absorption (perhaps a separate but associated component of “shielding gas” Gallagher & Everett 2007) moved into the line of sight some time after the *ROSAT* All Sky Survey observation, and before the *HST* and *FUSE* observations. On the other hand, as shown in §4.1.3, the gas that produces the UV BALs can nicely explain the *Swift* X-ray spectrum. Since we have only two epochs of UV spectroscopic data, with no

simultaneous X-ray coverage, it is difficult to determine precisely what happened.

Clearly, we need more observations to understand what is happening in WPVS 007. These are now even more urgent with the discovery from *Swift* that the absorption in the X-ray band is apparently changing. A second *FUSE* observation was approved, and even though WPVS 007, with a declination of -51 was in the region of the sky that could be observed after the loss of the reaction wheels, the observation was never scheduled before the satellite was decommissioned. An observation using *HST* COS has been approved, along with a contemporaneous *Chandra* observation, and therefore we still have a chance of observing further absorption evolution of this interesting object.

5. Summary

We present optical and UV observations of the unusual transient AGN WPVS 007. This Narrow-line Seyfert 1 galaxy was observed to be as bright as an average AGN of its luminosity in the *ROSAT* All Sky Survey, but then nearly disappeared from the X-ray sky in subsequent observation. We present a reanalysis of the 1996 *HST* optical and UV spectrum, and an analysis of the 2003 *FUSE* observation. The principle results follow.

- We discovered the emergence of broad absorption line features between the *HST* and *FUSE* observations. In the *HST* observation, mini-BALs with $v_{max} \sim 900 \text{ km s}^{-1}$ and $FWHM \sim 550 \text{ km s}^{-1}$ were observed. In the *FUSE* observation, the mini-BALs were still present, and an additional BAL component with $v_{max} \sim 6000 \text{ km s}^{-1}$ and $FWHM \sim 3400 \text{ km s}^{-1}$ had appeared. While variability of absorption lines in BAL quasars and Seyfert galaxies is frequently seen, it is usually limited to changes in the apparent optical depth of the line. The change in the line strength described here is the most dramatic ever observed in an AGN.
- Using a template method of analysis, we obtain the apparent optical depths of the absorption lines, and derive corresponding ionic column densities for both the BALs seen in the *FUSE* spectrum, and the mini-BALs seen in both the *HST* and *FUSE* spectra. BALs are thought to be saturated and have potentially velocity-dependent partial covering, so the measured ionic column densities are lower limits. We then use *Cloudy* to try to obtain some information about the physical conditions of the absorbing gas. We use two different continua: one with $\alpha_{ox} = -1.28$, similar to that of a typical quasar with the same optical luminosity as WPVS 007, and one with $\alpha_{ox} = -1.9$, corresponding to the inferred intrinsic value from the recent hard X-ray detection by *Swift* (Grupe et al. 2008). For the BALs, we find that P V constrains

the column density and ionization parameter. For the $\alpha_{ox} = -1.28$ continuum, we find that $\log(U) \geq 0$, and $\log(N_H) \geq 23$. For the $\alpha_{ox} = -1.9$ continuum, we obtain approximately the same limit on the ionization parameter, but require $\log(N_H) \geq 22.2$. For the $\alpha_{ox} = -1.9$ continuum and $Z = 5$ metallicity, the column density lower limit becomes $\log(N_H) \geq 21.6$. The total column density is lower for the steeper (intrinsically X-ray weak) continuum because intermediate ionization ions (in particular P^{+4}) are produced at smaller column densities in gas illuminated by a steep SED compared with gas illuminated by a flat SED (e.g., Leighly et al. 2007). These large column density estimates are similar to those obtained previously for the P V quasar PG 1254+047 (Hamann 1998). Acceleration of these large column densities challenge radiative-line driving as a mechanism. We also point out that since the observed P V absorption can be explained by lower total column densities using an intrinsically X-ray weak spectrum, we might expect to find P V absorption preferentially more often (or stronger) in quasars that are intrinsically X-ray weak.

- The high ionization parameters and high column densities inferred for the BALs predict X-ray absorption, implying that BALQSOs should be observed to be soft X-ray weak, as they are (e.g., Brandt et al. 2000). In addition, a recent long *Swift* observation indicates that WPVS 007 is also intrinsically X-ray weak, and thus there are apparently two effects leading to the long-term X-ray faintness of WPVS 007. We find that for the X-ray normal $\alpha_{ox} = -1.28$ SED, the X-ray absorption is insufficient to explain the low *Chandra* and *Swift* count rates. However, for the intrinsically X-ray weak $\alpha_{ox} = -1.9$ SED, with or without enhanced abundances, the inferred absorption yields predicted count rates are only slightly higher than observed. The predicted X-ray spectra for $\alpha_{ox} = -1.9$ have a heavily absorbed hard component, and a soft component due to reduced opacity resulting from the high ionization parameter. Thus, they resemble the spectrum from the recent *Swift* observation, but cannot explain the *Chandra* observation in which only soft photons were detected (Grupe et al. 2008). It is possible that the absorption column may have been larger during the *Chandra* observation. Despite the fact that the *FUSE* and *Swift* observations were separated by four years, this consistency supports the idea that the X-ray weakness and the broad absorption lines both result from absorption in the same gas. The weakness in this argument is that WPVS 007 was already X-ray weak during the *HST* observation, before the UV BAL emerged.
- Given the luminosity of the object, an estimate of its black hole mass, the BAL terminal velocity V_{max} , the lower limit on the absorption column, and the fraction of the bolometric luminosity inferred to be absorbed in the outflow, we can estimate the launch radius for the outflow using Eq. 3 from Hamann (1998). We find a negative

radius for the $\alpha_{ox} = -1.9$ solar abundance result, indicating that there is insufficient momentum in the absorbed photons to accelerate the gas to the observed terminal velocity. The largest launch radius (2.2×10^{15} cm) was obtained from the $\alpha_{ox} = -1.9$, $Z = 5$ model, which predicted the lowest estimated column density. However, this launch radius is a fraction (1/14) of the estimated size of the broad-line region, implying that we must not see it at the launch radius, but rather it crosses our line of sight further downstream. On the other hand, if the BAL outflows originate at larger radius than the BELR, it appears that radiative line driving is insufficient to accelerate the outflow, and a form of magnetic driving may be necessary.

- All other known cases of broad absorption lines are in luminous quasars. WPVS 007 has a uniquely low luminosity compared with other objects with similar V_{max} . It is therefore a significant outlier on the M_V/V_{max} relationship (Fig. 13, Laor & Brandt 2002).
- Given that there are only two epochs of UV spectroscopic observations of WPVS 007, one without and one with the BAL, it is impossible to determine the nature of the absorption variability. It may be a change in covering fraction due to a wind from an accretion disk orbiting into the line of sight, as has been suggested to explain variability in other BALs (Gibson et al. 2008). But given WPVS 007's low luminosity, quite unusual for an object with BAL $v_{max} \sim 6000 \text{ km s}^{-1}$, and correspondingly small size scales, it is possible that we have observed the development and onset of the BAL outflow. An approved *HST* observation using COS may help us understand the variability evolution in this unusual object.

KML is grateful for useful discussion with Mike Crenshaw, Xinyu Dai, and Steve Kraemer. We are also grateful that Mike Crenshaw, knowing that we were working on this paper, opted not to include it in the compilation of *FUSE* spectra from AGN and quasars (Dunn et al. 2007). Part of the work presented here was done while KML was on sabbatical at the Department of Astronomy at The Ohio State University, and she thanks the members of the department for their hospitality. OU graduate student Hemantha Maddumage and 2006 OU REU student Curtis McCully performed the reduction of the XMM-Newton EPIC data from Mrk 493 and Mrk 335. This research was supported by NASA contracts NAG5-13701 (K.M.L. & D.C.) and NNX07AH67G (D.G.). The authors also thank an anonymous referee who's comments lead to greater clarity in the paper. Some of the data presented in this paper were obtained from the Multimission Archive at the Space Telescope Science Institute (MAST). STScI is operated by the Association of Universities for Research in Astronomy, Inc., under NASA contract NAS5-26555. Support for MAST for non-HST data is

provided by the NASA Office of Space Science via grant NAG5-7584 and by other grants and contracts. This research has made use of the NASA/IPAC Extragalactic Database (NED) which is operated by the Jet Propulsion Laboratory, California Institute of Technology, under contract with the National Aeronautics and Space Administration. This research has made use of data obtained from the High Energy Astrophysics Science Archive Research Center (HEASARC), provided by NASA’s Goddard Space Flight Center. KML and DAC gratefully acknowledge support by NASA grant NAG5-13701 (FUSE).

Facilities: FUSE, HST (FOS)

A. FUSE Data Processing and Background Subtraction

The data were processed with CalFUSE version 3.1.8. The standard procedure circa summer 2006 was followed. First, the “jitter” files were repaired using the command `cf_jitter` and the CalFUSE pipeline was run on the individual segments of the observation. Then, the command `idf_combine` was run to combine the segments, setting the “-c” flag in order to recompute the centroids of the spectral traces in the final intermediate data file (IDF). At the same time, the bad pixel maps were combined using `bpm_combine`. These steps were run for data taken at night alone, and for the combined day-and-night data.

At this point, the data are ready to have the spectrum extracted and calibrated, and the background model constructed and the background subtracted. All of this is done by the CalFUSE script `cf_extract_spectra`. AGN are faint sources for *FUSE*, so a high-quality background subtraction is essential. The data reduction and background subtraction pipeline for *FUSE* has improved dramatically over the years (Dixon et al. 2007). However, the background subtraction algorithms do not fully exploit an important fact: the background has a different PHA (pulse height analyzer) spectrum than the source photons. To illustrate this, we display in Fig. 14 the PHA distributions for the source region and the background region for the LIF1a data. Specifically, we extracted the data from the bow-tie LIF1a extraction region found in the `spex1a009.fit` file given in CalFUSE version 2.4 (the extraction regions are handled differently in CalFUSE 3.1 and greater), and the histogram of PHA is shown as a solid line. The dashed line shows the PHA distribution from background regions of the detector that avoid the apertures and airglow lines, scaled to area of the source aperture, and therefore approximately giving the distribution of background in the source aperture. This background is an estimate for two reasons: 1.) the scattered light is more intense in the aperture, a fact that would increase the estimation of the background; 2.) the regions of the detectors under the apertures have lost sensitivity over the years, a fact that

would decrease the estimation of the background. At any rate, it can clearly be seen that the background dominates for PHA channels less than 2 and greater than 20, and we can reduce the background and therefore increase the statistics of the spectrum by excluding these PHA channels. Note that we are not the first to reduce the background by imposing a PHA restriction (e.g., Brotherton et al. 2002; Casebeer, Leighly & Baron 2006).

The background files provided by the *FUSE* team have been carefully constructed. Each one is comprised of ~ 20 background observations, and they vary stepwise in time to account for periodically imposed gain changes. But they have been constructed for the default PHA range, and although they are scaled in the background modeling process, in principle the shape of the background spectrum should change depending on the PHA range.

We decided therefore to construct our own background images using the following restricted PHA ranges: 1a: 5–20; 1b: 9–22; 2a: 3–14; 2b: 6–20. These were determined as shown in Fig. 14; we plotted background and source regions, and determined the range of PHA in which the source dominates. To construct the background images, first we determined the appropriate background observations from the lists in the headers of the background files produced by the *FUSE* team. For our observation, there were 24 separate observation IDs that were used in constructing the background images. In general, the background is different during orbital day and orbital night; the scattered background is a little higher in the day, plus there are more and stronger airglow lines, and therefore we construct separate background images for day and night. These various observation segments ranged from 765 seconds to 23345 seconds in duration; we excluded the very lowest exposure observation from the 2a and 2b detectors, therefore we used only 23 files to construct the backgrounds for each of those detectors.

For each detector and each segment, the following processing steps were done. The day and night intermediate data files were extracted using the *FUSE* IDL program `cf_edit`, and at the same time the pha restriction was applied. In *CalFUSE* 3.1 and higher, all events are retained in the data files, and bad data (e.g., from flaring or jitter, i.e., when the target is not in the aperture) are marked using flags. We extracted the flag information from the fits files, and then use that information to separate out the good day or night events. An image can be plotted using the good events.

The image of each background file contains airglow lines, with the day image having more lines and more intense lines. We do not want the intense lines in the background, so we exclude regions of the image with strong lines. The flags aid this selection as there is a flag for airglow feature. A mask is made of the excluded regions. Next, the extracted images are added together, day and night separately, weighted by the exposure time and the airglow mask. Regions with a fractional exposure less than 0.3 of the total exposure

time are excluded from the background region. The day and night background images are convolved with a gaussian kernel with a FWHM of 15 pixels, and a constant is subtracted. Finally, the images are output as fits files in the same format as those produced by the *FUSE* team (indeed with the same headers, with exposure times altered). These files are available online⁹.

These background files can be used in two ways. First, they can be directly used in the CalFUSE script `cf_spec_extract` by copying them to the `calfiles` directory, and changing the `BKGD_CAL` keyword in the primary header of the IDF file from which the spectrum will be extracted. At the same time, `PHALOW` and `PHAHIGH` keywords should be changed to match those of the background files. The scaling factors for the day and night data, plus the constant, can be extracted from the verbose output of `cf_spec_extract`.

Fig. 15 shows the results of our background subtraction compared with the default. To construct these figures, we first determined the y-direction ranges on the image in which the light from the target or scattered emission is not seen, i.e., we avoid the LWRS apertures and mostly the MDRS aperture as well. In addition, regions at the edge of the detector where the background is exceptionally high were also avoided. “Spectra” were constructed by summing the events along the spatial direction, and binning by a factor of 16 in the dispersion direction. These spectra were extracted from the day+night data from WPVS 007 (black lines) and from the modeled background data, using the scale factors obtained from the `cf_spec_extract` output (red lines). It can be readily seen that the background-modeled spectra from our files match the data better. In fact, in the case of the 2b detector, the `cf_spec_extract` modeling appears to have failed for the default data, as the day and night scaling factors were zero, and the background was a constant; the background modeling did not fail for these data for our background files.

While Fig. 15 shows that the PHA-limited backgrounds perform perfectly well in `cf_spec_extract`, there is another way to use these background files. The background spectra were extracted from the WPVS 007 data as above, and day and night background spectra were extracted from the model files over the same background regions. Then, the WPVS 007 background spectra were fit using the IRAF task `Specfit` to a model consisting of the day background spectrum, the night background spectrum, and a constant. Regions where the flux is zero (i.e., beyond the edges of the detector) and regions where strong airglow lines are present were excluded from the fit. The normalizations of the day and night files were constrained to be in proportion to their respective exposure times. Then, the `Specfit` results could be input directly into a modified version of the `cf_spec_extract` program. The result is shown

⁹http://www.nhn.ou.edu/leighly/FUSE_bkgd

in the right panel as the green line in Fig. 15. It differs only slightly from the result obtained using `cf_spec_extract` directly.

Fig. 16 shows the a comparison of the LIF spectra extracted using the default PHA ranges and `cf_spec_extract` program with spectra obtained using the restricted PHA range and the new background files scaled using the `Specfit` fitting described above. We show both the day-and-night spectra in dark grey, and night-only spectra in light grey. The chief utility of the night-only spectra is the identification of airglow lines in the day-and-night spectra. In addition, the less prominent airglow lines are seen only in the day data, so they can be removed by substituting the night-only spectra in those regions. Overall, there is not much difference between the default and the PHA-restricted spectra, even though the background levels are 5–40% lower for the PHA-restricted spectra. There are detailed differences, however. For example, the 1b day-and-night spectra do not agree in normalization with the night-only spectra for the default reduction, while they do for the PHA-restricted reduction. In addition, the failure of the background subtraction for the day-and-night Lif2b data is apparent for the default reduction.

Fig. 17 shows a similar plot for the SIC data. In this case, only the night spectra are shown. The SIC has a much lower effective area (a factor of three) than the LIF, and it is difficult to obtain useful results from these detectors for a faint object like WPVS 007. This can be seen by comparing the spectrum around 1065Å in the LIF1a spectrum in Fig. 16, and the same region in the SIC1a spectrum. However, the SIC spectra extend to shorter wavelengths; in particular, a feature is clearly detected near 980Å in both the SIC1b and SIC2a spectra. Again, overall, the differences between the default spectra and the restricted-PHA spectra are small; however, the restricted PHA spectra are slightly less noisy, and approach zero more gracefully (e.g., SIC2a for wavelengths shorter than 960Å).

B. Merging the *FUSE* Spectra

The *FUSE* observation yields eight separate spectra, and we proceed here to merge them. WPVS 007 is a faint object for *FUSE* and as the SIC telescope/detector systems have effective areas about 1/3 of the LIF, the SIC spectra have rather low signal-to-noise ratios (Fig. 17). Thus, we use those data only for the shortest wavelength ranges where LIF spectra are not available.

The longest wavelengths are sampled by the LIF 1b and LIF 2a. LIF 1b is commonly afflicted by the “worm”, or shadowing of the grid wires on the detector (Sahnou 2002). Our spectra are no exception, as can be seen by the difference in the 1b and 2a spectra longward

of $\sim 1140 \text{ \AA}$ (Fig. 16). The worm decreases the effective area, decreasing also the signal-to-noise ratio, and therefore we opt to ignore afflicted region. We average the two spectra in overlapping region ($1094.25\text{--}1137.25 \text{ \AA}$), and use the 2a spectrum longward of that. The errors are computed by propagation in quadrature.

We turn next to the region of the spectrum between 987.5 and 1074.75 \AA , which are represented by both the LIF 1a and LIF 2b spectra. The LIF 2b spectrum has generally a poorer signal-to-noise ratio than the LIF 1a spectrum, as seen in Fig. 16, and the question arises, do we enhance or degrade the signal-to-noise ratio of the LIF1a spectrum by averaging it with the LIF2b spectrum? We also find that the normalization of the 2b spectrum appears to be about 15% lower than the 1a spectrum. Since at the time of this observation, the pointing was still being determined using the LIF1a detector, we assume that it has the correct normalization. We examine the mean spectrum and decide to use the mean of the LIF1a and LIF2b scaled by a factor of 1.15 between 1011 and 1074.75 \AA . The LIF1a contains useful information longward of the merged region, to $\sim 1082.5 \text{ \AA}$, and there is a gap between the coverage of LIF1a and the coverage of LIF2b from ~ 1082.5 to $\sim 1087 \text{ \AA}$. In principle, the SIC 2b could be used to fill this gap; however, examination of Fig. 17 shows there is no signal in this region in that spectrum.

Shortward of 1100 \AA , we use the LIF1a, SIC1b, and SIC2a spectra, as follows. The LIF1a nominally extends down to 987.5 \AA , but as can be seen in Fig. 16, the signal-to-noise ratio approaches 1 at the shortest wavelengths. The SIC2a overlaps up to 1005.5 \AA , but again, the errors are large at the end of the spectrum. We use LIF1a alone down to 1002.75 \AA , and use the mean of LIF1a and SIC2a between 995.5 and 1002.5 \AA . Shortward of that, the spectrum is represented by SIC2a until 992.5 \AA , when it is joined by SIC1b. The uncertainty on the SIC1b spectrum is very large at the end, so we use the SIC2a alone down to 987.75 \AA . Shortward of that, we use the mean of the SIC1b and SIC2a spectra down to 920 \AA .

There are several prominent airglow lines remaining in the spectrum. These include the Lyman lines of hydrogen, $\text{Ly}\beta$ at 1025.722 \AA , $\text{Ly}\gamma$ at 972.537 \AA , and $\text{Ly}\delta$ at 949.743 \AA , and O I line near 988 \AA . The regions of the spectra in the vicinity of these lines are excised.

Finally, the spectra are modestly smoothed¹⁰, dereddened and shifted to the restframe.

REFERENCES

Aoki, K., Kawaguchi, T., & Ohta, K. 2005, ApJ, 618, 601

¹⁰The smoothing function is $0.2(f(i-1) + 3f(i) + f(i+1))$.

- Arav, N., et al. 2001, *ApJ*, 61, 118
- Arav, N., et al. 2007, *ApJ*, 658, 829
- Barlow, T. A., 1994, *PASP*, 106, 548
- Bentz, M. C., Peterson, B. M., Pogge, R. W., Vestergaard, M., & Onken, C. A. 2006, *ApJ*, 644, 133
- Bian, W., Yuan, Q., & Zhao, Y. 2005, *MNRAS*, 364, 187
- Bottoff, M., Korista, K. T., Shlosman, I., & Blandford, R. D., 1997, *ApJ*, 479, 200
- Brandt, W. N., Laor, A., & Wills, B. J. 2000, *ApJ*, 528, 637
- Brotherton, M. S., Tran, H. D., Becker, R. H., Gregg, M. D., Laurent-Muehleisen, S. A., & White, R. L. 2001, *ApJ*, 546, 775
- Brotherton, M. S., Green, R. F., Kriss, G. A., Oegerle, W., Kaiser, M. E., Zheng, W., & Hutchings, J. 2002, *ApJ*, 565, 800
- Cardelli, J. A., Clayton, G. C., & Mathis, J. S. 1989, *ApJ*, 345, 245
- Cavaliere, A., Lapi, A., & Menci, N. 2002, *ApJ*, 581, L1
- Constantin, A., & Shields, J. C. 2003, *PASP*, 115, 592
- Cohen, R. D. 1983, *ApJ*, 273, 489
- Collin, S., Kawaguchi, T., Peterson, B. M., & Vestergaard, M. 2006, *A&A*, 456, 75
- Crenshaw, D. M., Kraemer, S. B., Boggess, A., Maran, S. P., Mushotzky, R. F., & Wu, C.-C., 1999, *ApJ*, 516, 750
- Crenshaw, D. M., Kraemer, S. B., Bruhweiler, F. C., & Ruiz, J. R. 2001, *ApJ*, 555, 633
- Crenshaw, D. M., et al. 2002, *ApJ*, 566, 187
- Casebeer, D. A., Leighly, K. M., & Baron, E. 2006, *ApJ*, 637, 157
- Dixon, W. V., et al., *PASP*, 119, 527
- Dunn, J. P., Crenshaw, D. M., Kraemer, S. B., & Gabel, J. R., 2007, *AJ*, 134, 1061
- Dunn, J. P., Jackson, B., Deo, R. P., Farrington, C., Das, V., & Crenshaw, D. M. 2006, *PASJ*, 118, 572

- Everett, J. E., 2005, ApJ, 631, 689
- Ferland, G. J., Korista, K. T., Verner, D. A., Ferguson, J. W., Kingdon, J. B., & Verner, E. M. 1998, PASP, 110, 761
- Gallagher, S. C., Brandt, W. N., Chartas, G., Priddey, R., Garmire, G. P., & Sambruna, R. M. 2006, ApJ, 644, 709
- Gallagher, S. C., & Everett, J. E. 2000, ASPC, 373, 305
- Gibson, R. R., Brandt, W. N., Schneider, D. P., & Gallagher, S. C., 2008, ApJ, 675, 985
- Goodrich, R. W., 2000, NewAR, 44, 519
- Grevesse, N., Asplund, M., & Sauval, A. J., 2007, Space Sci. Rev. 130, 105
- Grupe, D., Beuerman, K., Mannheim, K., Thomas, H.-C., Fink, H. H., & de Martino, D., 1995, A&A, 300, L21
- Grupe, D., Leighly, K. M., & Komossa, S. 2008, AJ136, 2343
- Grupe, D., Schady, P., Leighly, K. M., Komossa, S., O’Brien, P. T., & Nousek, J. A. 2007, accepted for publication in AJ, astro-ph/0701564
- Hamann, F., ApJS, 109, 279
- Hamann, F., ApJ, 500, 798
- Hamann, F., & Ferland, G. 1999, ARA&A, 37, 487
- Hamann, F. W., Barlow, T. A., Chafee, F. C., Foltz, C. B., & Weymann, R. J. 2001, ApJ, 550, 142
- Hamann, F., Korista, K. T., Ferland, G. J., Warner, C., & Baldwin, J. 2002, ApJ, 564, 592
- Junkkarinen, V. T., Burbidge, E. M., & Smith, H. E. 1983, ApJ, 265, 51
- Hamann, F., Sabra, B., Junkkarinen, V., Cohen, R. & Shields, G. 2001, proc. “X-ray Spectroscopy of AGN with *Chandra* and *XMM-Newton*”, eds. T. Boller, S. Komossa, S. Kahn, & H. Kunieda (MPE Report), astro-ph/0304564
- Hamann, F., Kaplan, K. F., Rodriguez Hidalgo, P., Prochaska, J. X., & Herbert-Fort, S. 2008, MNRAS, 391, L39
- Junkkarinen, V. T., Cohen, R. D., Hamann, F., & Shields, G. A., 2001, BAAS, 33, 897

- Kuraszkiewicz, J. K., Green, P. J., Crenshaw, D. M., Dunn, J., Forster, K., Vestergaard, M., & Aldcroft, T. L., 2004, *ApJS*, 150, 165
- Laor, A. & Brandt, W. N. 2002, *ApJ*, 569, 641
- Leighly, K. M., 1999, *ApJS*, 125, 317
- Leighly, K. M. 2004, *ApJ*, 611, 125
- Leighly, K. M., Halpern, J. P., Jenkins, E. B., & Casebeer, D. 2007, *ApJS*, 173, 1
- Leighly, K. M., & Moore, J. R. 2004, *ApJ*, 611, 107
- Leighly, K. M., & Moore, J. R. 2006, *ApJ*, 644, 748
- Lundgren, B. F., Wilhite, B. C., Brunner, R. J., Hall, P. B., Schneider, D. P., York, D. G., Vanden Berk, D. E., & Brinkmann, J., 2007, *ApJ*, 656, 73
- Ma 2002, *MNRAS*, 335, L99
- Morrison, R. & McCammon, D. 1983, *ApJ*, 270, 119
- ApJS*, 77, 119
- Narayanan, D., Hamann, F., Barlow, T., Burbidge, E. M., Cohen, R. D., Junkkarinen, V., & Lyons, R. 2004, *ApJ*, 601, 715
- Phillips, M. M. 1976, *ApJ*, 208, 37
- Poole, T. S., et al. 2008, *MNRAS*, 383, 627
- Prévot, M. L., Lequeux, J., Maurice, E., Prévot, L., & Rocca-Volmerange, B. 1984, *A&A*, 132, 389
- Proga, D., in “The Central Engine of Active Galactic Nuclei”, eds L. C. Ho & J.-M. Wang (ASP: San Francisco), p. 267
- Rodriguez Hidalgo, P., Hamann, F., Nestor, D., Shields, J. 2007, *ASPC*, 373, 287
- “The FUSE Instrument and Data Handbook”, Ed. D. Sahnou, <http://fuse.pha.jhu.edu/analysis/IDH/IDH.html>
- Saraph, H. E., & Storey, P. J. 1999, *A&AS*, 134, 369
- Savage, B. D., Sembach, K. R. 1991, *ApJ*, 379, 245

- Scannapieco, E., & Oh, S. P. 2004, ApJ, 608, 62
- Schegel, D. J., Finkbeiner, D. P., & Davis, M. 1998, ApJ, 500, 525
- Steffen, A. T., Strateva, I., Brandt, W. N., Alexander, D. M., Koekemoer, A. M., Lehmer, B. D., Schneider, D. P., & Vignali, C. 2006, AJ, 131, 2826
- Vaughan, S., Edelson, R., Warwick, R. S., 2004, MNRAS, 349, 1
- Weingartner, J. D., & Draine, B. T. 2001, ApJ548, 296
- Zheng, W., Kriss, G. A., Telfer, R. C., Grimes, J. P., & Davidsen, A., ApJ, 475, 469

Table 1. Observing Log

Spectrometer	Date	Exposure (seconds)	Bandpass (Å)	Aperture ^a	Resolution (Å)
<i>HST</i> FOS (G130H)	1996-07-30	3840	1140–1606	0.86''	2.26
<i>HST</i> FOS (G190H)	1996-07-30	1500	1590–2312	0.86''	3.16
<i>HST</i> FOS (G1270H)	1996-07-30	1280	2222–3277	0.86''	4.72
<i>HST</i> FOS (G1400H)	1996-07-30	1000	3235–4781	0.86''	6.94
<i>HST</i> FOS (G570H)	1996-07-30	630	4569–6818	0.86''	10.06
<i>FUSE</i> LIF1a	2003-11-06	47354	987.5–1082.5	30''	0.25 ^b
<i>FUSE</i> LIF1b	2003-11-06	48054	1094.25–1188.75	30''	0.25 ^b
<i>FUSE</i> LIF2a	2003-11-06	48229	1087.0–1181.25	30''	0.25 ^b
<i>FUSE</i> LIF2b	2003-11-06	48466	980.0–1074.75	30''	0.25 ^b
<i>FUSE</i> SIC1a	2003-11-06	35055	1003.25–1090.5	30''	0.25 ^b
<i>FUSE</i> SIC1b	2003-11-06	35259	904.25–992.5	30''	0.25 ^b
<i>FUSE</i> SIC2a	2003-11-06	34982	917.5–1005.5	30''	0.25 ^b
<i>FUSE</i> SIC2b	2003-11-06	35010	1016.75–1103.5	30''	0.25 ^b

^aFor the *HST* FOS spectra, this refers to the size of the round aperture. For the *FUSE* spectra, this refers to the size of the LWRS square aperture.

^bThe observed resolution of *FUSE* using the LWRS aperture is $R = 20,000 \pm 2000$ (The *FUSE* Observer’s Guide: <http://fuse.pha.jhu.edu/support/guide/guide.html>). However, the low count rate cannot sample this resolution. Therefore, the resolution refers to the final binsize of the spectra.

Table 2. Estimated Column Densities

Ion	Wavelength (Å)	Scale Factor	Template ^a	$\log(N)^b$ (cm^{-2})
P IV	950.66	3.08 ± 0.38	P V	$> 15.19 \pm 0.05$
P IV	950.66	1.33 ± 0.58	O VI MiniBAL	$> 14.31 \pm 0.20$
Ly γ^c	972.54	2.17 ± 0.31	P V	$> 16.77 \pm 0.06$
C III	977.03	2.61 ± 0.37	P V	$> 15.43 \pm 0.06$
C III	977.03	1.28 ± 0.23	O VI MiniBAL	$> 14.60 \pm 0.08$
C III ^d	977.03	1		> 15.87
N III ^c	990.98	2.38 ± 0.09	P V	$> 15.87 \pm 0.02$
N III ^c	990.98	0.88 ± 0.23	O VI MiniBAL	$> 14.93 \pm 0.12$
P III	998.00	< 0.27	P V	< 15.26
P III	1001.73	0.59 ± 0.25	P V	$> 15.60 \pm 0.19$
P III	1003.60	0.77 ± 0.29	P V	$> 15.72 \pm 0.17$
S III	1012.50	1.10 ± 0.34	P V	$> 16.29 \pm 0.14$
S III ^c	1015.63	1.26 ± 0.47	P V	$> 16.35 \pm 0.17$
S III ^c	1021.32	1.28 ± 0.46	P V	$> 16.35 \pm 0.16$
Ly β^c	1025.72	2.72 ± 0.46	P V	$> 16.41 \pm 0.07$
Ly β^c	1025.72	3.89 ± 3.0	O VI MiniBAL	$> 16.05 \pm 0.44$
O VI	1031.91	1.68 ± 0.28	P V	$> 15.97 \pm 0.07$
O VI	1037.61	2.41 ± 0.15	P V	$> 16.43 \pm 0.03$
O VI	1031.91	3.0 ± 1.1	O VI MiniBAL	$> 15.71 \pm 0.17$
O VI	1037.61	1.99 ± 0.25	O VI MiniBAL	$> 15.83 \pm 0.06$
O VI ^d	1033.68	1		> 16.64
S IV	1062.66	1.20 ± 0.05	P V	$> 15.17 \pm 0.02$
S IV ^c	1073.03	1.54 ± 0.03	P V	$> 15.27 \pm 0.01$
S IV ^{c,e}	1073.03	< 0.046	O VI MiniBAL	< 13.24
N II ^{c,e}	1085.12	0.09 ± 0.02	P V	$> 13.77 \pm 0.11$
P V	1117.98	1.30 ± 0.04	P V	$> 15.29 \pm 0.01$
P V	1128.01	0.89 ± 0.04	P V	$> 15.43 \pm 0.02$
P V ^e	1128.01	< 0.09	O VI MiniBAL	< 13.95
Fe III ^{c,e}	1125.79	< 0.17	P V	< 13.77
Ly α^c	1215.67	0.95 ± 0.05	N V MiniBAL	$> 12.31 \pm 0.02$

Table 2—Continued

Ion	Wavelength (Å)	Scale Factor	Template ^a	$\log(N)^b$ (cm^{-2})
N V	1238.82	1.07 ± 0.13	N V MiniBAL	$> 12.78 \pm 0.05$
N V	1242.80	0.94 ± 0.11	N V MiniBAL	$> 13.02 \pm 0.05$
C IV	1548.20	1.27 ± 0.10	N V MiniBAL	$> 12.67 \pm 0.03$
C IV	1550.77	1.59 ± 0.09	N V MiniBAL	$> 13.05 \pm 0.03$

^aDevelopment of the three templates are described in the following sections: P V in §3.1; O VI MiniBAL in §3.2; N V MiniBAL in §2.3.

^bThe ionic column densities were obtained from the apparent optical depths and therefore are lower limits. The detections are denoted using $>$, and the uncertainties reflect the statistical uncertainty on the determination of the lower limit in the spectral fitting.

^cWhen the line is comprised of multiplets indistinguishable at the spectral resolution, the column densities were estimated using the sum of the f_{12} for the multiplets.

^dColumn density obtained using the alternative deblending described in §3.3.4. No template is used.

^eUpper limits on lines that were not observed.

Table 3. Estimated X-ray 0.3–10 keV Count Rates

Model	<i>Chandra</i>				<i>Swift</i>			
	direct rate	direct counts ^a	absorbed rate	absorbed counts ^a	direct rate	direct counts ^b	absorbed rate	absorbed counts ^b
$\alpha_{ox} = -1.28; N_H = 23.0$	1.53	14192	0.049	454	0.15	12599	0.0038	325
$\alpha_{ox} = -1.9; N_H = 22.2$	0.032	300	0.0061	56	0.0090	764	0.0011	91
$\alpha_{ox} = -1.9, Z = 5; N_H = 21.6$	0.032	300	0.0045	41	0.0089	764	0.00083	71

^aThe effective exposure of the *Chandra* observation was 9300 seconds, and 10 net source photons were observed.

^bThe effective exposure of the *Swift* observation was 85,508 seconds (Grupe et al. 2008), and 35.7 net source photons were observed.

Table 4. Dynamics Components

Model	L_{46} ^a	L/L_{Edd} ^b	$F_{0.1}$ ^c	N_{22} ^d	$R_{0.1}$ ^e
$\alpha_{ox} = -1.28$	0.0114	0.22	4.1	10.0	0.0031
$\alpha_{ox} = -1.9$	0.0049	0.096	0.67	1.58	< 0
$\alpha_{ox} = -1.9, Z = 5$	0.0049	0.096	0.44	0.40	0.0070

Note. — We use a black hole mass $M_8 = 0.041$ estimated from the optical luminosity and the $H\beta$ line width (Collin et al. 2006). We use a terminal velocity $V_\infty = 4000 \text{ km s}^{-1}$ estimated from the apparent optical depth shown in Fig. 4.

^aThe bolometric luminosity in units of $10^{46} \text{ erg s}^{-1}$ obtained by integrating over the *Cloudy* input continua discussed in §4.1.1 after normalizing to the *HST* spectrum in the optical band.

^bThe ratio of the bolometric luminosity to the the Eddington luminosity obtained using the black hole mass estimate $M_8 = 0.041$.

^cThe fraction of the continuum absorbed by the wind, estimated by integrating over the absorbed continuum, and divided by 0.1.

^dThe lower limit on the column densities obtained in §4.1.2 in units of 10^{22} cm^{-2} .

^eThe launch radius in units of 0.1 pc estimated using Eq. 3 in Hamann (1998).

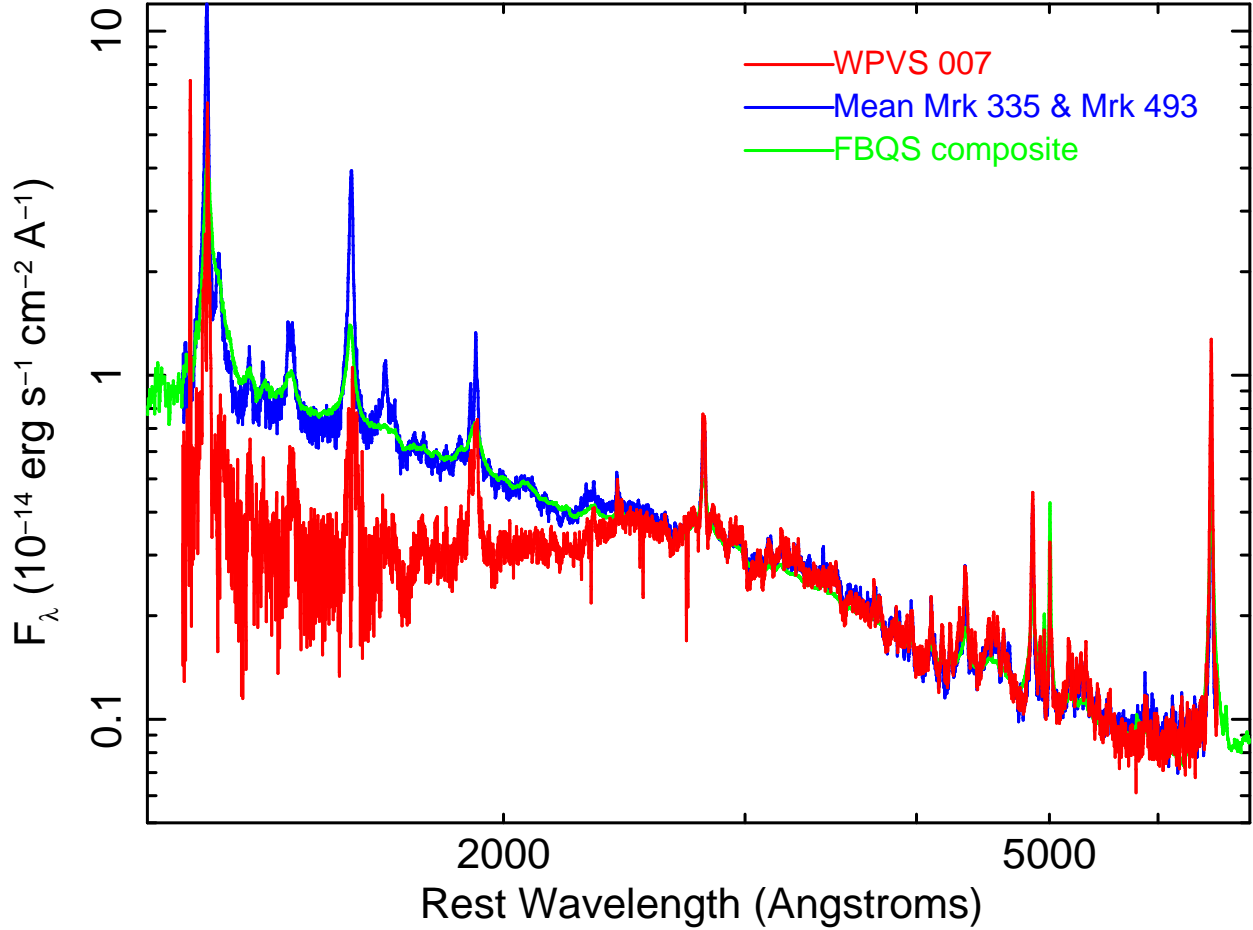


Fig. 1.— The *HST* WPVS 007 spectrum (red) overlaid on the mean of the *HST* spectra from two NLS1s Mrk 335 and Mrk 493 (blue) and the FBQS radio-quiet composite spectrum (Brotherton et al. 2001).

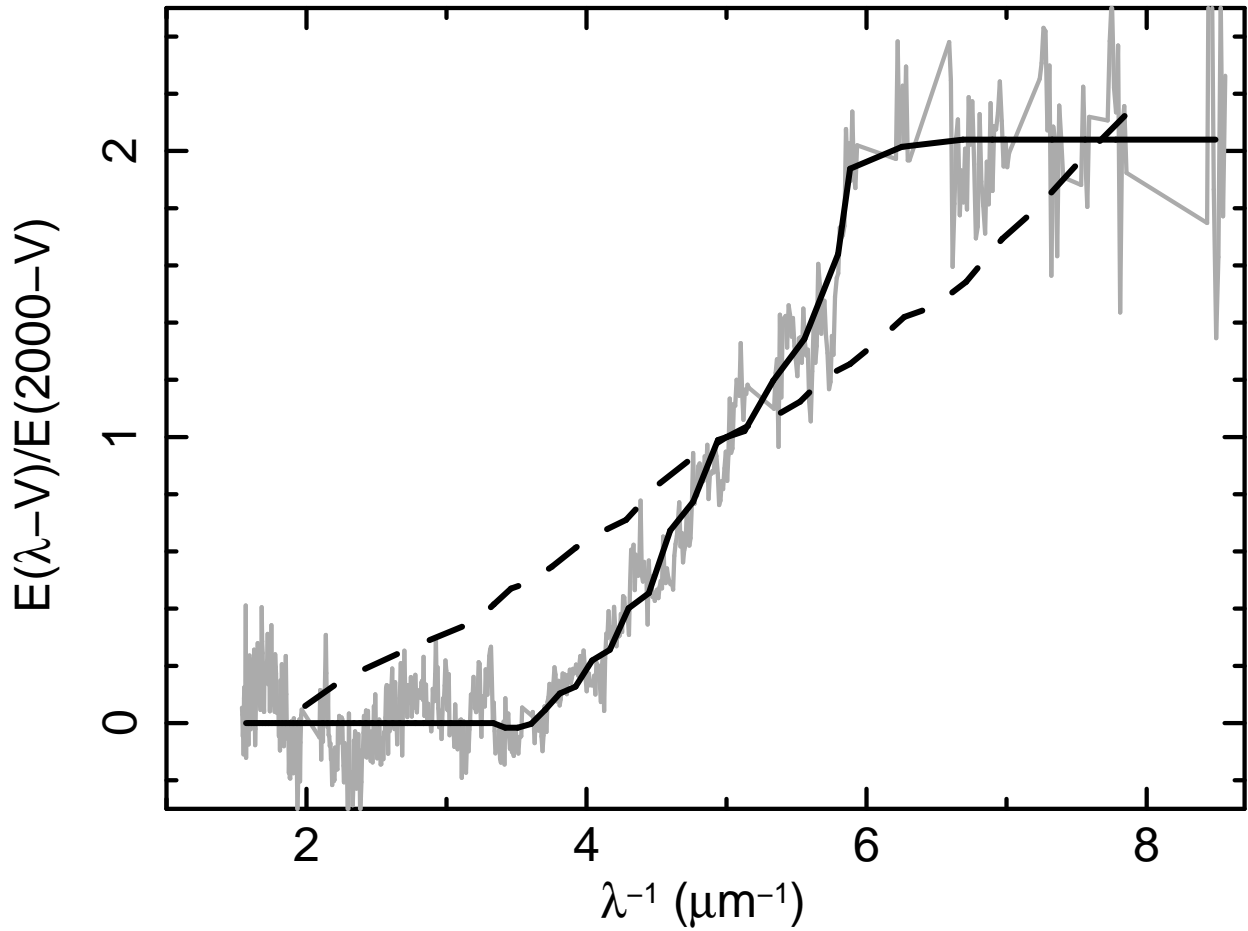


Fig. 2.— Reddening curve for WPVS 007. The grey line shows the ratio of the WPVS 007 spectrum with the average NLS1 spectrum obtained from Mrk 335 and Mrk 493. The solid black line shows a spline fit to the ratio spectrum. The dashed black line shows the SMC reddening curve (Prévot et al. 1984).

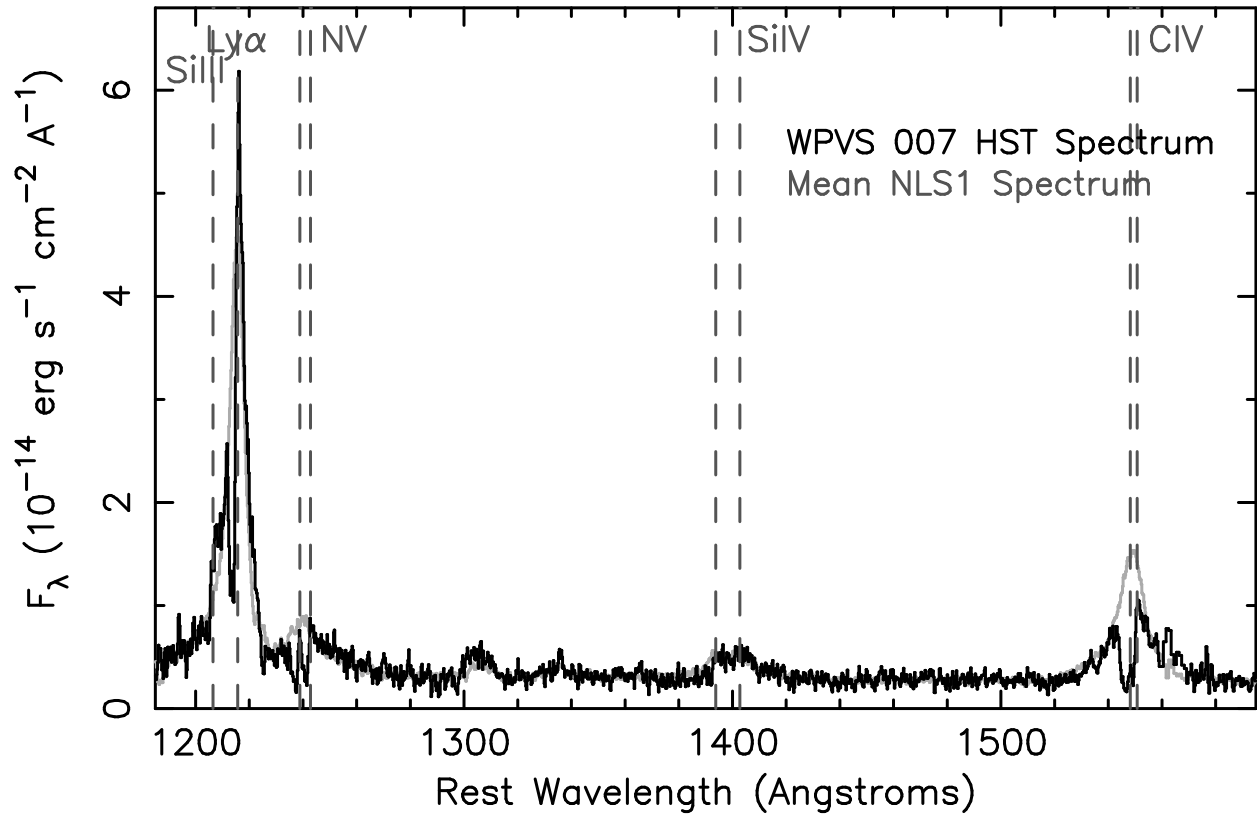


Fig. 3.— The merged *HST* spectrum from WPVS 007 in comparison with the mean NLS1 spectrum created from the *HST* spectra of the NLS1s Mrk 335 and Mrk 493. Absorption lines are clearly present on Ly α , N V, and C IV.

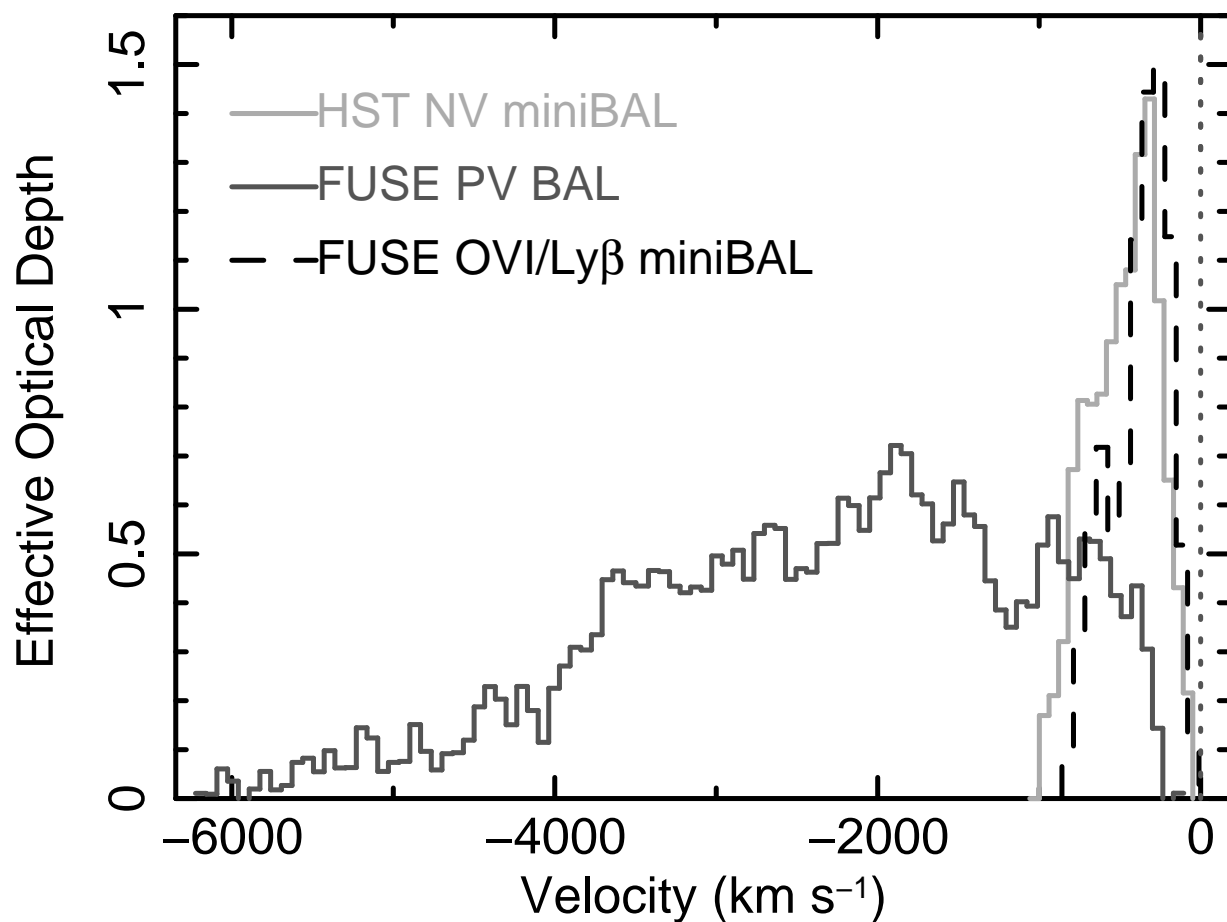


Fig. 4.— The extracted optical depths as a function of velocity for the N V mini-BAL, extracted from the *HST* spectrum (§2.3), the P V BAL, extracted from the *FUSE* spectrum (§3.1) and the O VI/Ly β mini-BAL, extracted from the *FUSE* spectrum (§3.2). Note the difference in onset velocity between the BAL and the mini-BALs. There is some indication that the shape of the mini-BAL changed between the *HST* and *FUSE* observations; however, given the uncertainty in continuum placement and background subtraction, those differences may not be significant.

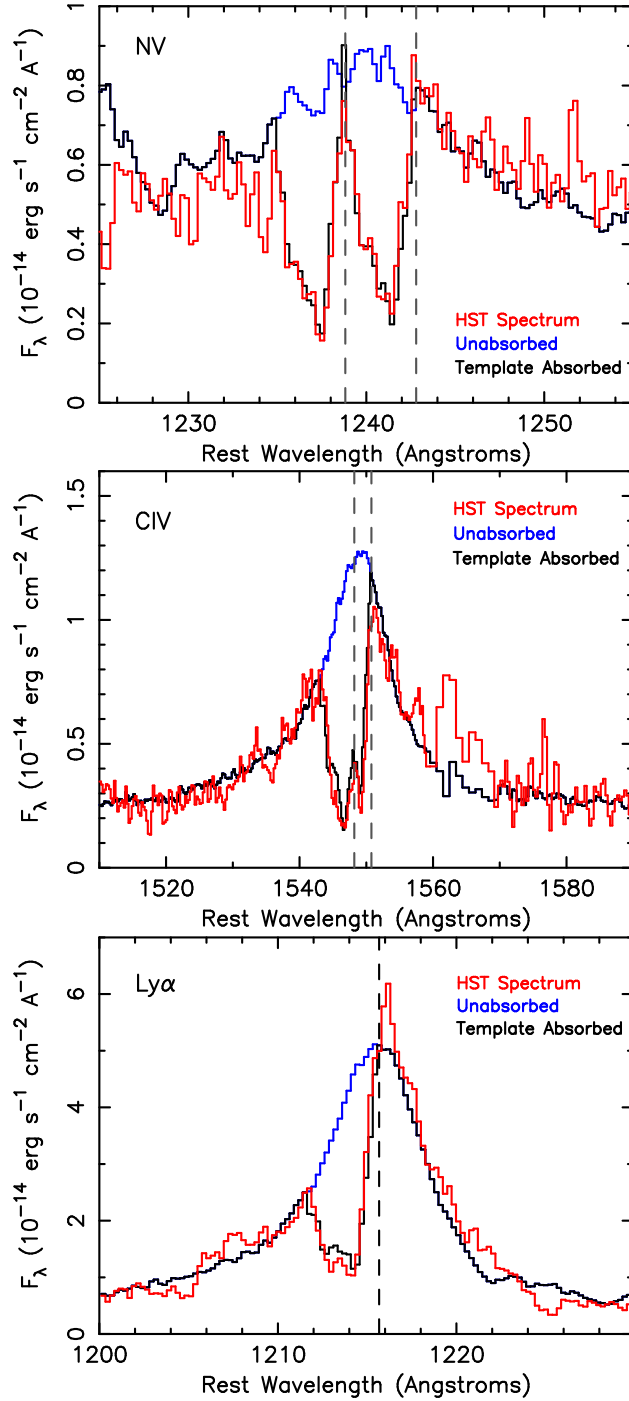


Fig. 5.— Absorption lines in the *HST* spectrum (red lines) compared with the mean NLS1 spectrum (blue lines). Top: The absorption line template was created from the well-resolved N V absorption lines using the procedure described in §2.3. It was then applied to the mean NLS1 spectrum created from the the *HST* spectra of Mrk 335 and Mrk 493 (black lines). Assuming that the absorption lines are optically thick and have the same profile for all lines, we apply the template created from the N V absorption lines to the C IV line (middle) and Ly α line (bottom).

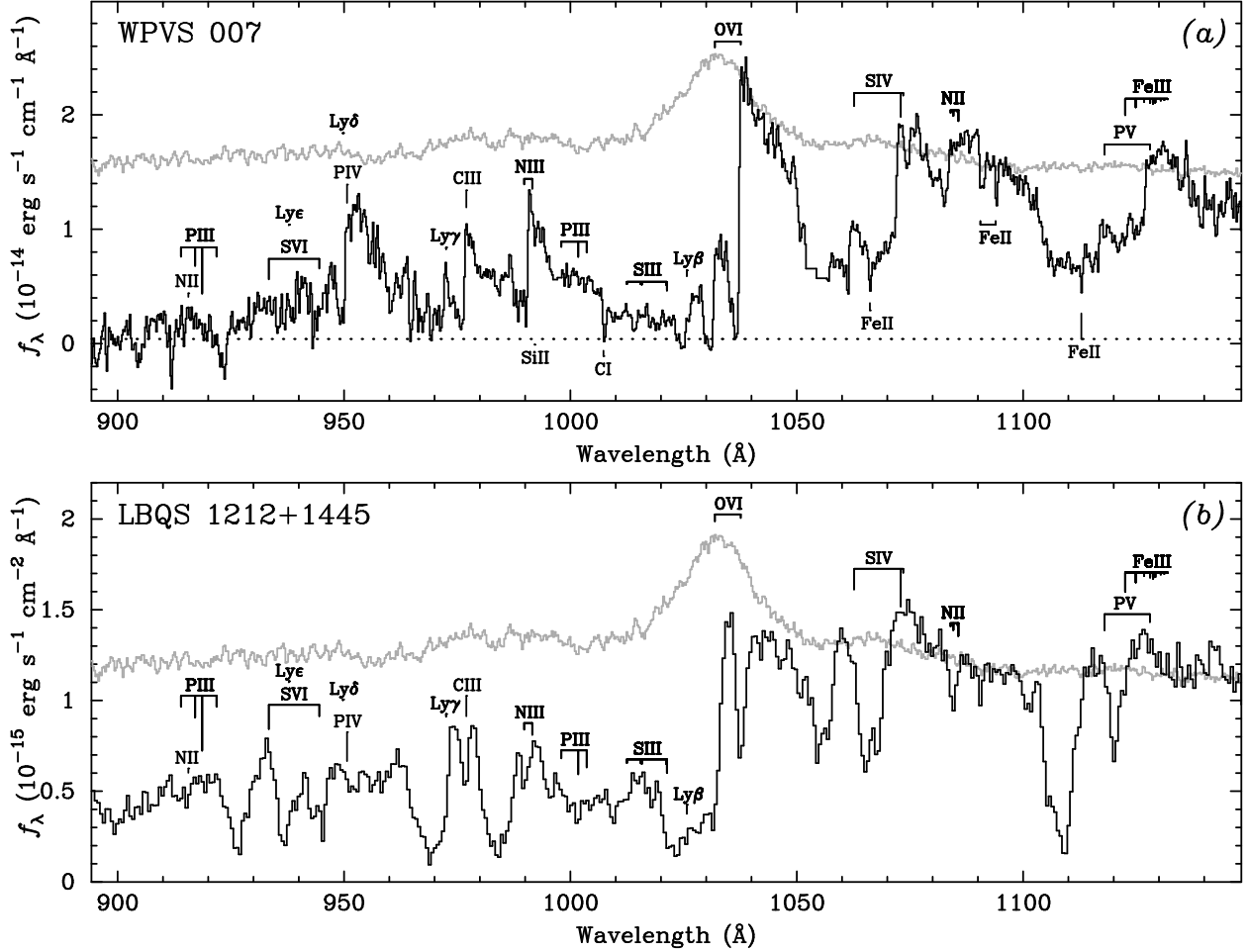


Fig. 6.— (a) The merged, smoothed, dereddened, and deredshifted *FUSE* spectrum of WPVS 007 (black line). For comparison, the scaled *HST* quasar composite spectrum is shown. Identified Galactic absorption lines are marked below the spectrum. Rest wavelengths of prominent emission lines in the bandpass are labeled above the spectrum, regardless of whether or not the corresponding absorption is observed. Length of tick marks are proportional to gf for individual multiplets. (b.) The *HST* STIS spectrum of the P V BALQSO LBQS 1212+1445 for comparison.

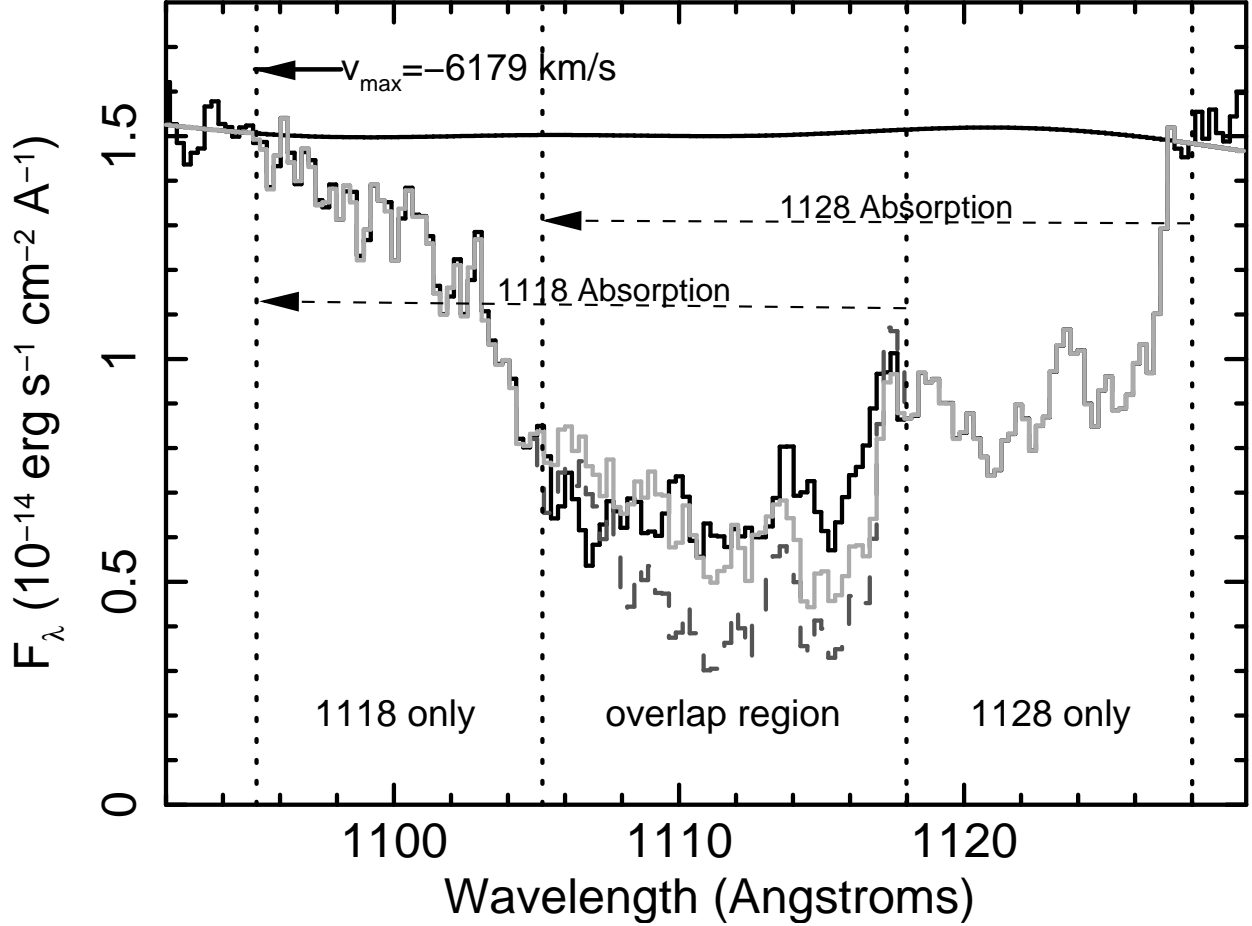


Fig. 7.— The analysis of the P V region of the *FUSE* spectrum. The spectrum is shown by the black line. The continuum, a spline fit to the scaled *HST* composite spectrum (Zheng et al. 1997), is shown by the nearly horizontal black line. The vertical dotted lines delineate the regions of the absorption profile either represented by only the 1118Å component of P V (left), by only the 1128Å component of P V (right), and by both (middle). V_{max} shows the high-velocity extent of the BAL inferred from the 1118Å component. The dashed dark grey line shows the inferred spectrum if the apparent optical depth of the 1118Å component is 2.03 times the apparent optical depth of the 1128Å component, as would be appropriate if the gas were optically thin and partial covering were negligible. The light grey line shows the results of apparent optical depth fitting described in §3.1. The ratio of the apparent optical depths was 1.35. See text for details.

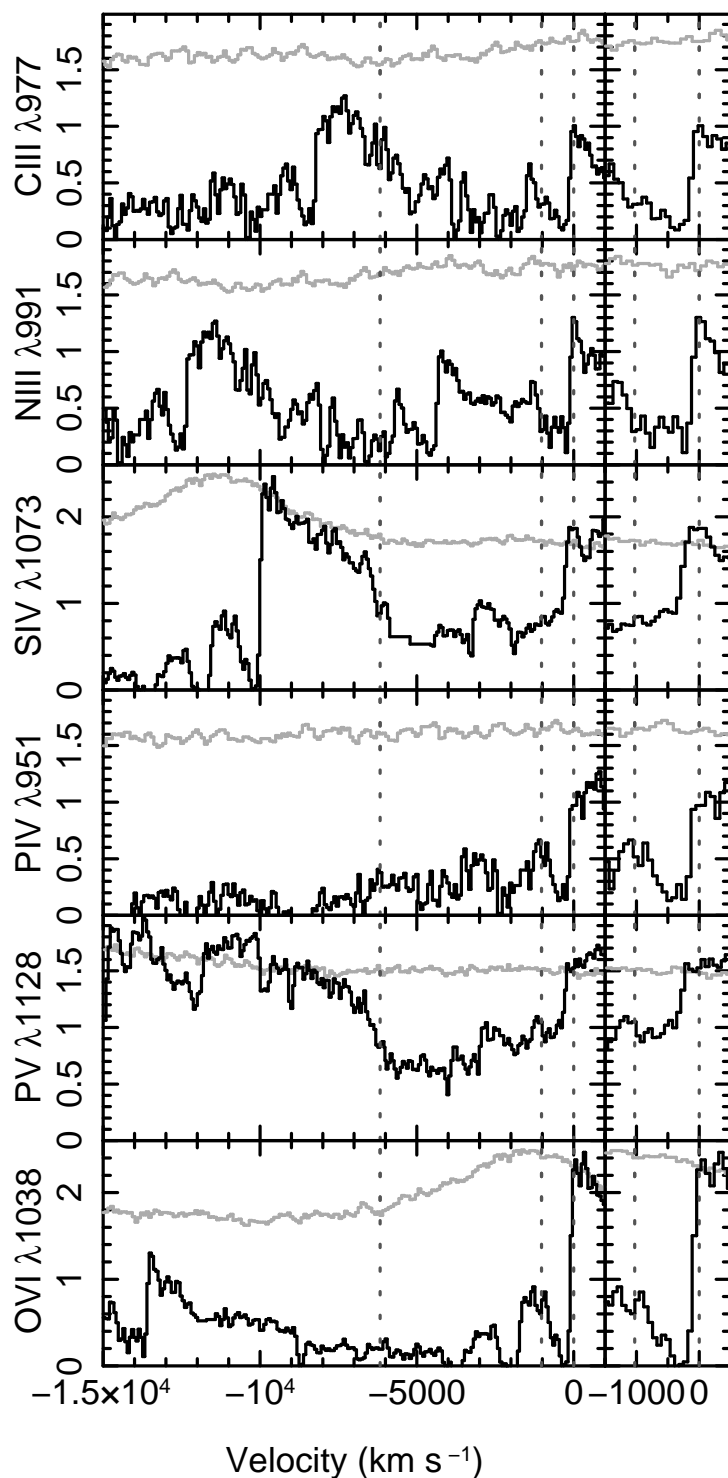


Fig. 8.— The *FUSE* spectrum plotted as a function of velocity relative to various absorption line rest wavelengths. The light grey lines show the scaled *HST* composite spectrum (Zheng et al. 1997). The right side shows an expanded view of the low-velocity region. Note the overall similarity between the S IV and the P V profiles; the absorption blueward of O VI is much broader. In addition, the onset of the P V and S IV absorption occurs at higher velocity than the other lines, indicating that the mini-BAL is not present in P V and S IV.

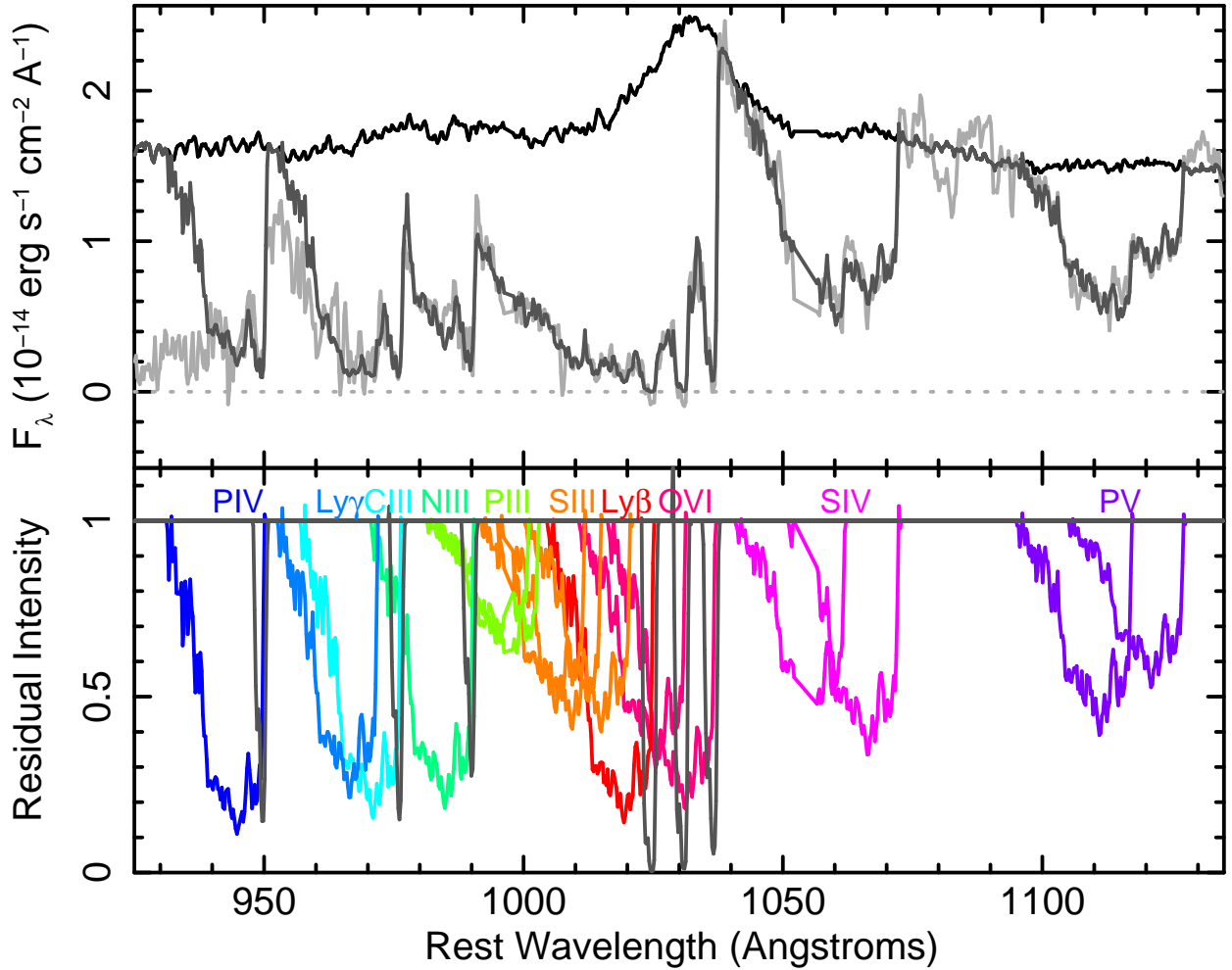


Fig. 9.— The spectral fit derived in §3.3.1, 3.3.2, and 3.3.3. Top panel: the light grey line shows the data, the black line shows the assumed continuum, and the dark grey line shows the model fit comprised of the BAL template created from P V (§3.1) and the mini-BAL template created from O VI and $\text{Ly}\beta$ (§3.2). The fit in the region of S IV is very good and validates the approach. The fit in the region of O VI is good also, but a large number of transitions and ions are needed. As described in §3.3.3, we failed to fit the region between 950 and 958 Å, suggesting that the $\text{Ly}\gamma$ or C III is broader than the P V BAL, that the assumed continuum level is incorrect and should be lower, or that there are unidentified ions contributing to this absorption feature. Bottom panel: The absorption features contributing to the fit shown in the top panel. For the P V template, the color of the absorption feature corresponds to the ion above the panel. Six incidences of the O VI miniBAL are fitted and are shown in grey; from left to right, they correspond to P IV, C III, N III, $\text{Ly}\beta$, and two O VI.

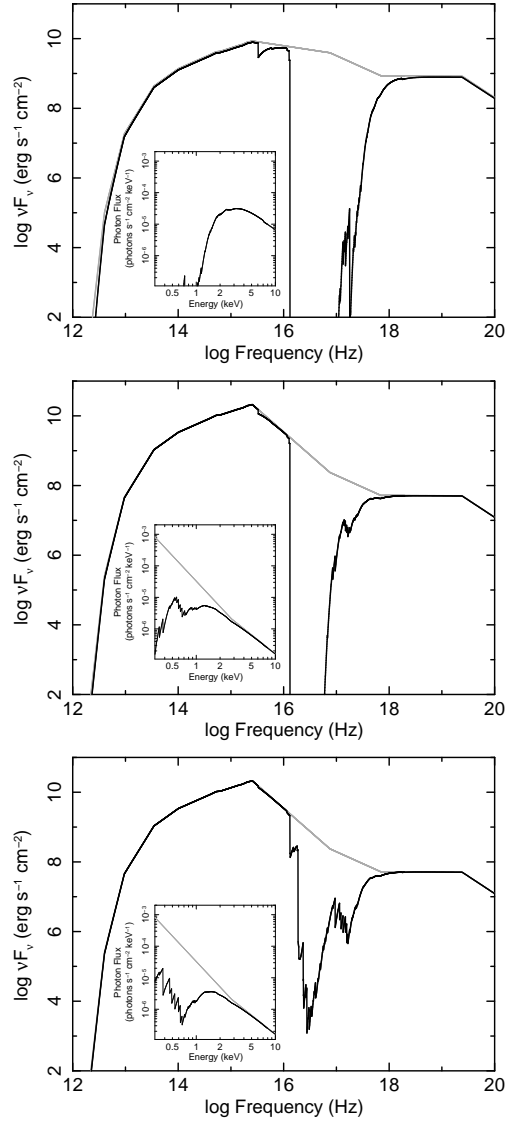


Fig. 10.— Continua used for *Cloudy* modeling (see §4.1.1; light grey) and inferred absorbed spectra (see §4.1.3; black). The inset plots show the X-ray bandpass photon flux units. Top: The continuum inferred using the *HST* and *XMM-Newton* observations of Mrk 335 and Mrk 493; this continuum has $\alpha_{ox} = -1.28$. The absorbing gas has $\log(U) = 0$, $\log(n) = 10.0$ and $\log(N_H) = 23.0$. Middle: The X-ray weak continuum inferred from the recent *Swift* hard X-ray detection of WPVS 007 (Grupe et al. 2008); $\alpha_{ox} = -1.9$. The absorbing gas has $\log(U) = 0$, $\log(n) = 10.0$, and $\log(N_H) = 22.2$. Bottom: The X-ray weak continuum again, but absorbed through metal-rich gas ($Z = 5$). The absorbing gas has $\log(U) = 0$, $\log(n) = 10.0$, and $\log(N_H) = 21.6$.

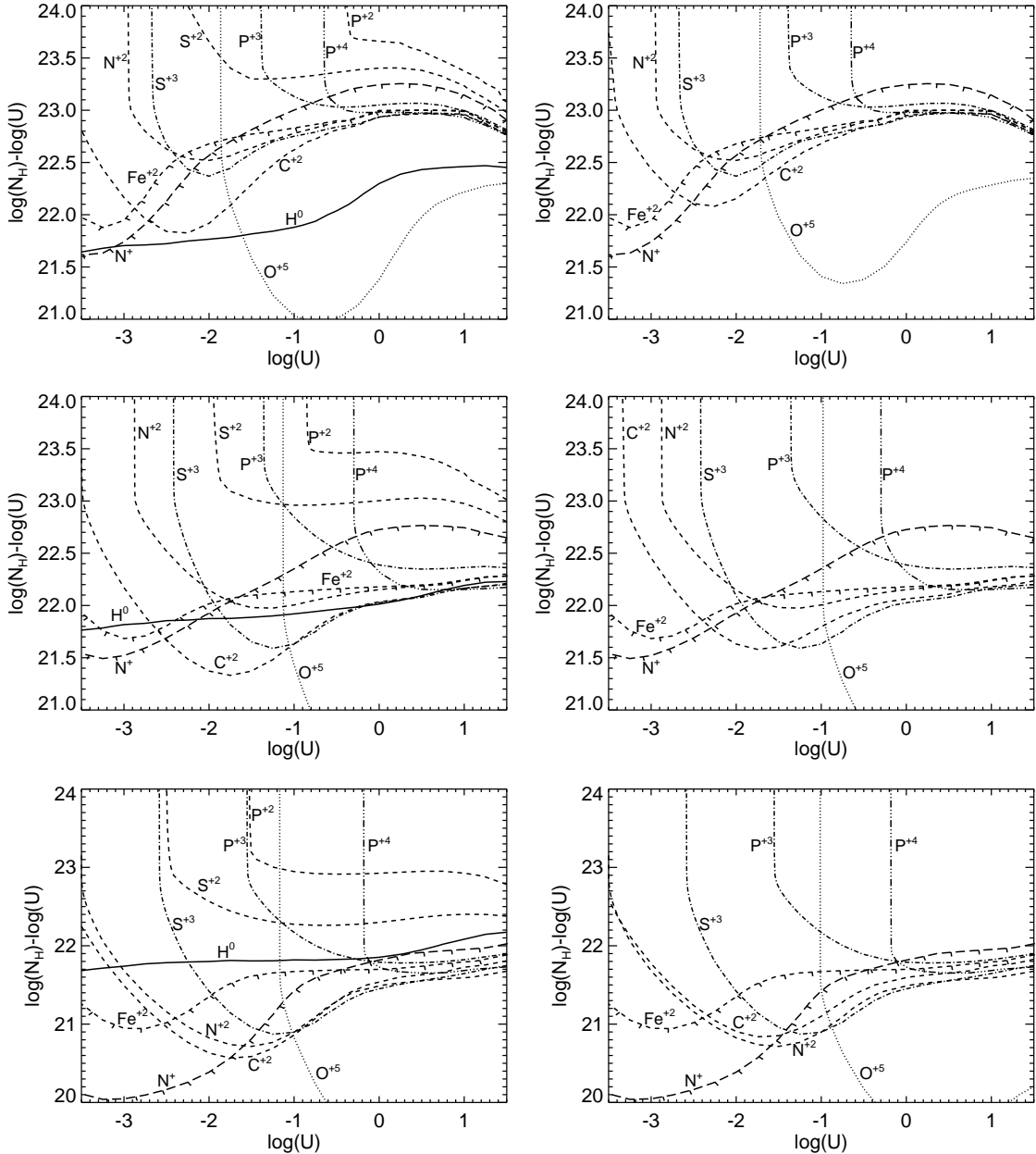


Fig. 11.— Contours of observed column densities on the $\log(N_H) - \log(U)$ versus $\log(U)$ plane for $\log(n) = 10.0$. These column densities were derived using the apparent optical depths, implying that they are lower limits and the real solution should lie above and to the right of any particular contour. The exceptions are the upper limits for lines that were not observed which are denoted by downward tick marks. Plots on the left use column densities from the deblending using only the *FUSE* BAL template (and O VI/Ly β mini-BAL template) shown in Fig. 9; plots on the right use column densities from the alternative deblending discussed in §3.3.4. The top, middle and bottom panels have the same meaning as in Fig. 10. The line style shows the ionization state: dotted for +5, dot-dot-dot-dash for +4, dot-dash for +3, short dash for +2, long dash for +1, and solid for neutral.

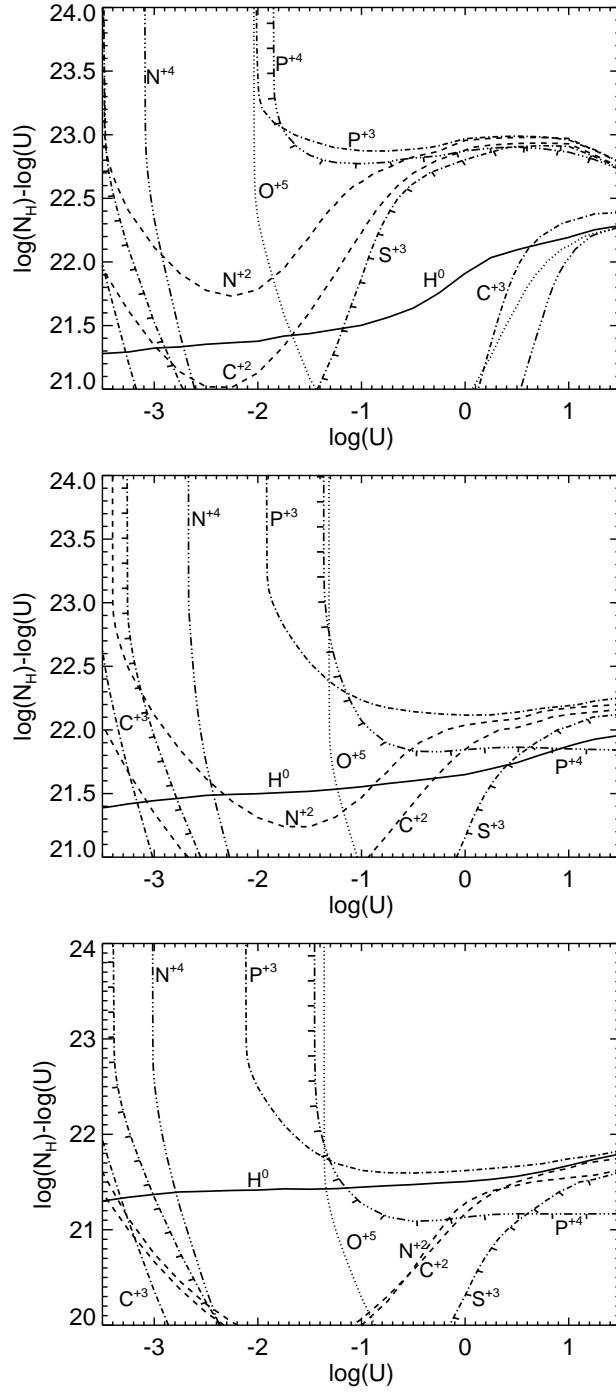


Fig. 12.— Contours of observed column densities on the $\log(N_H) - \log(U)$ versus $\log(U)$ plane for $\log(n) = 10.0$ for the mini-BALs. Lines have the same meaning as in Fig. 11.

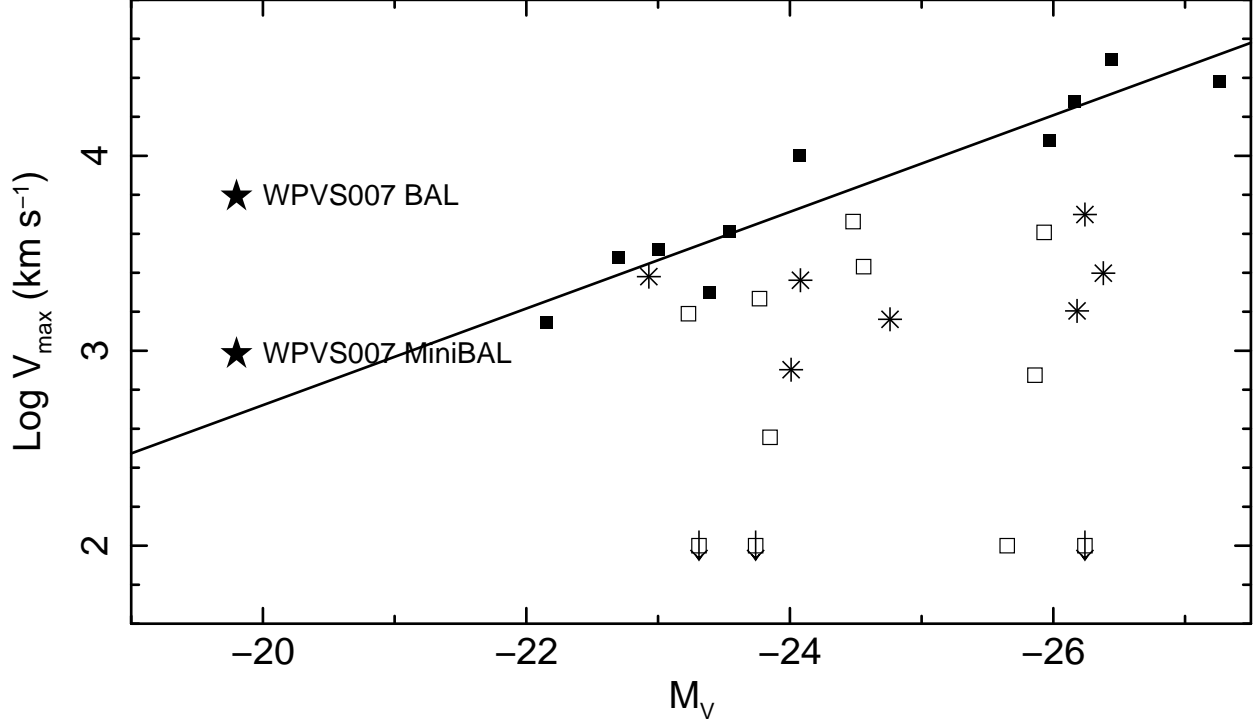


Fig. 13.— WPVS 007 in comparison with low-redshift quasars presented by Laor & Brandt (2002). This is an adoption of their Fig. 6 and the data was taken from their Table 1. The symbols are taken from their paper with the insubstantial modification that we do not differentiate between objects with data in C IV and objects with data in Ly α , as follows: filled squares are soft X-ray weak quasars (SXWQs), asterisks are non-SXWQs with intermediate absorption ($1\text{\AA} < \text{EW} < 10\text{\AA}$), open squares are AGN with weak absorption ($\text{EW} < 1\text{\AA}$), and arrows are objects with $V_{max} < 10 \text{ km s}^{-1}$. The solid line is the regression to the SXWQ data presented by Laor & Brandt (2002). In addition, we plot our results from the *HST* and *FUSE* observation of WPVS 007. The filled star marked “WPVS 007 BAL” shows the V_{max} from the *FUSE* BAL template derivation presented in §3.1. It lies far above the regression, indicating a rather large maximum velocity for its luminosity. The filled star marked “WPVS 007 MiniBAL” shows the mean of the V_{max} for the *HST* and *FUSE* mini-BALs derived in §2.3 and 3.2, respectively. The mini-BAL V_{max} is more consistent with that expected of an object of WPVS 007’s luminosity.

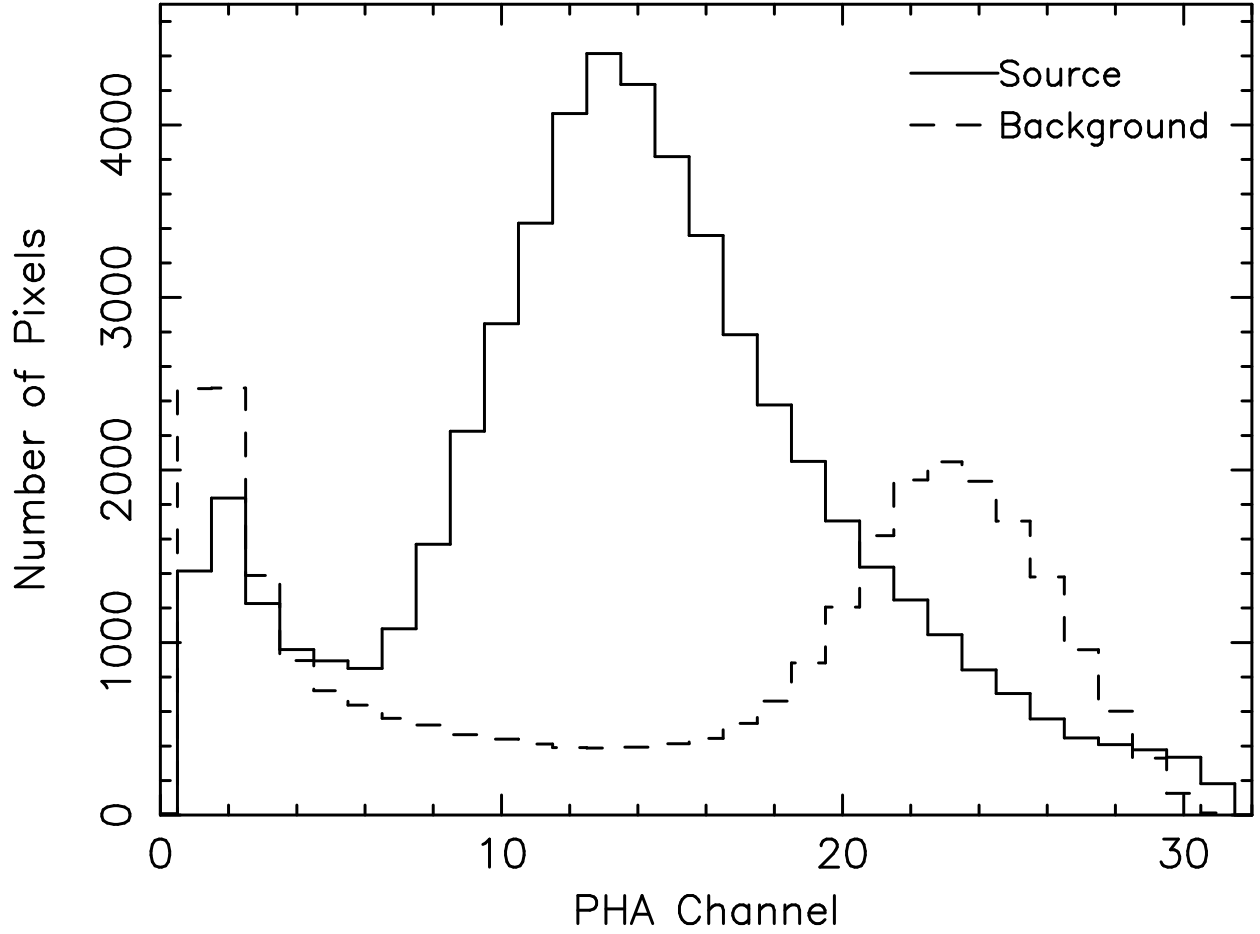


Fig. 14.— Distribution of PHA from events lying in the source lif1a “bowtie” extraction region (solid line) and background regions scaled to the area of the source region (dashed line).

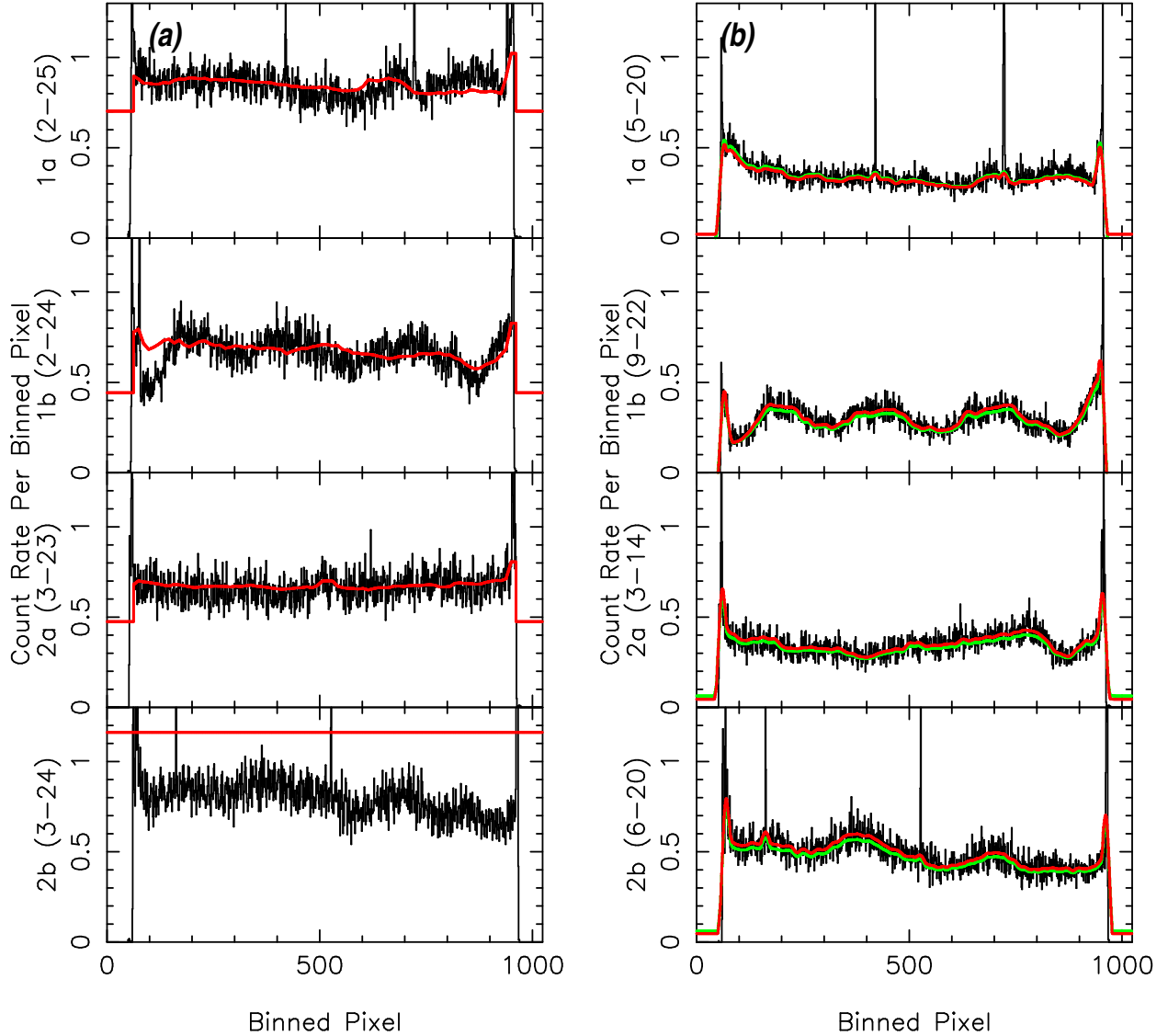


Fig. 15.— Background spectra were created from the regions of the detectors avoiding the LWRS and MDRS apertures and high background regions near the edges of the detectors. Background spectra were created from the background images over the same background regions. Those background regions were scaled using either the `cf_extract_spectra` output (red lines) or using the results from `Specfit` modeling (green line; see text for details). (a.) the default spectra and pha selection; (b.) the spectra from the new background images created by us using pha selection. The background is lower when the PHA is restricted in range, and the background spectra model the data better.

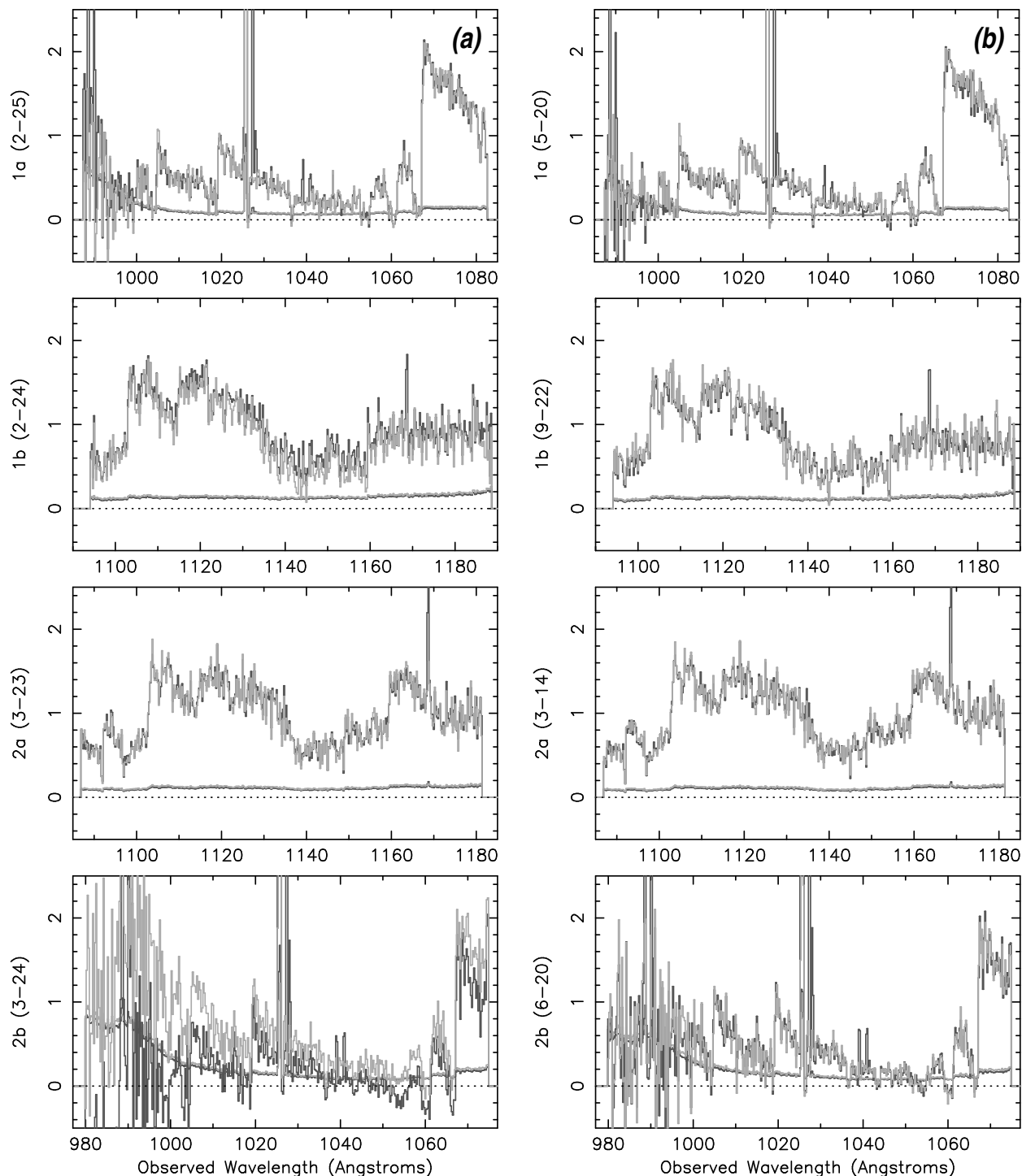


Fig. 16.— Comparison of LIF spectra extracted using default PHA ranges and background images (left, (a)) with spectra extracted using the restricted PHA range and the new background images (right, (b)). Day-and-night spectra are shown in dark grey, and night-only spectra are shown in light grey. In both cases, the uncertainty is shown as a line below the spectra for clarity. These figures show that overall there is not very much difference between the default and new spectra.

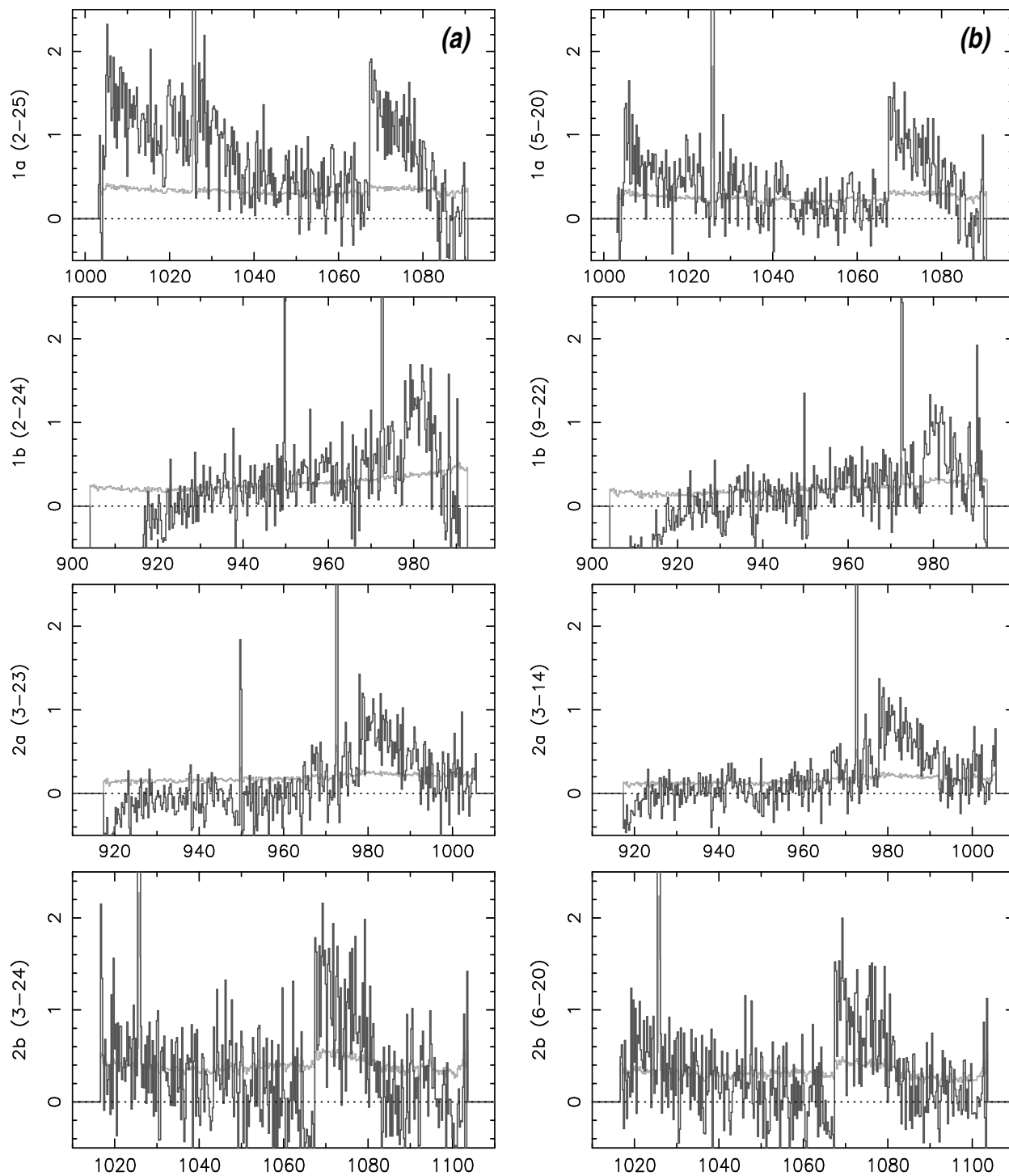


Fig. 17.— Similar to Fig. 16 for the SIC spectra. The left panel (a) shows the spectra extracted using default PHA ranges and background images; the right panel (b) shows the spectra extracted with the restricted PHA range and new background. In both cases, night-only spectra are shown.